Distinct pathway for evolution of enhanced receptor binding and cell entry in SARS-like bat coronaviruses

Alexandra L. Tse[1+], Cory M. Acreman[2+], Inna Ricardo-Lax[3], Jacob Berrigan[1], Gorka Lasso[1], Toheeb Balogun[4], Fiona L. Kearns[4], Lorenzo Casalino[4], Georgia L. McClain[3], Amartya Mudry Chandran[1], Charlotte Lemeunier[1], Rommie E. Amaro[4], Charles M. Rice[3], Rohit K. Jangra[1,6], Jason S. McLellan[2++], Kartik Chandran[1++*], Emily Happy Miller[1,5++]

+ Co-first
++ Co-corresponding
* Lead contact

[1] Department of Microbiology & Immunology, Albert Einstein College of Medicine, Bronx, NY, USA.
[2] Department of Molecular Biosciences, The University of Texas at Austin, Austin, TX, USA.
[3] Laboratory of Virology and Infectious Disease, The Rockefeller University, New York, NY, USA
[4] Department of Molecular Biology, University of California – San Diego, La Jolla, CA, USA
[5] Department of Medicine, Albert Einstein College of Medicine, Bronx, NY, USA.
[6] Present address: Department of Microbiology and Immunology, Louisiana State University Health Sciences Center-Shreveport, Shreveport, LA, USA.

ABSTRACT

Understanding the zoonotic risks posed by bat coronaviruses (CoVs) is critical for pandemic preparedness. Herein, we generated recombinant vesicular stomatitis viruses (rVSVs) bearing spikes from divergent bat CoVs to investigate their cell entry mechanisms. Unexpectedly, the successful recovery of rVSVs bearing the spike from SHC014, a SARS-like bat CoV, was associated with the acquisition of a novel substitution in the S2 fusion peptide-proximal region (FPPR). This substitution enhanced viral entry in both VSV and coronavirus contexts by increasing the availability of the spike receptor-binding domain to recognize its cellular receptor, ACE2. A second substitution in the spike N–terminal domain, uncovered through forward-genetic selection, interacted epistatically with the FPPR substitution to synergistically enhance spike:ACE2 interaction and viral entry. Our findings identify genetic pathways for adaptation by bat CoVs during spillover and host-to-host transmission, fitness trade-offs inherent to these pathways, and potential Achilles' heels that could be targeted with countermeasures.

INTRODUCTION

The recent emergence of multiple human coronaviruses—SARS-CoV, MERS-CoV, and SARS-CoV-2—accompanied by disease epidemics of regional or global scope, has highlighted the urgent need to identify related animal coronaviruses (CoVs), understand their biology and zoonotic potential, and pre-position countermeasures. Efforts to sample and sequence CoVs circulating in nature have identified a diverse, globally distributed group of viruses in bats.[1–3] Studies performed with authentic coronaviruses, pseudotyped viral vectors bearing bat-origin CoV spikes, and/or recombinant spike proteins have shown that many of these agents can enter and infect human cells, pointing to bats as major reservoirs for novel CoVs with the potential for zoonotic transmission to humans.[4–14] However, these findings have also demonstrated a continuum of cell entry efficiencies that could not be fully explained by differences in spike:receptor binding affinity alone, indicating the existence of additional entry barriers to human infection by some bat-origin CoVs.[3,5,15–19]

As a case in point, a large sequencing study conducted in horseshoe bats collected from Yunnan Province, China, isolated seven distinct full-length CoV sequences belonging to the subgenus of SARS-like betacoronaviruses (sarbecoviruses), including two from novel agents—Rs3367 and RsSHC014—and determined their full-length genome sequences.[4] The authors also recorded the first successful isolation of a replication-competent SARS-like CoV (SL-CoV), WIV-1, that was almost identical to SL-CoV Rs3367 in sequence and demonstrated that it could replicate in human cells. However, they could not recover a virus corresponding to RsSHC014-CoV (hereafter, SHC014-CoV) from bat fecal samples. Interestingly, although later studies showed that the receptor-binding domains (RBDs) of both WIV-1 and SHC014 CoV spikes could recognize human angiotensin-converting enzyme-2 (ACE2)—the cell entry receptor for SARS-CoV, SARS-CoV-2, and many other sarbecoviruses—with high affinity,[20,21] Menachery and colleagues reported that only the WIV-1 spike could mediate high levels of lentiviral vector transduction into cells over-expressing human ACE2.[13] Indeed, they measured little or no activity for the SHC014-CoV spike in this assay. Unexpectedly, however, authentic CoVs

bearing the SHC014-CoV spike could be rescued by reverse genetics, replicated in human airway cultures, and were virulent in mice, leading the authors to conclude that, despite their results with pseudotyped viruses, the SHC014-CoV spike was 'poised' to mediate infections in humans.[13] Subsequent studies have incorporated SHC014-CoV spike pseudotypes into larger panels of single-cycle viruses for analyses of antibody-mediated neutralization but have not investigated their entry-related properties in detail,[22–25] leaving open questions about potential molecular incompatibilities between this and other bat-origin CoV spikes and human cells.

The coronavirus spike glycoprotein, S, forms homotrimers embedded in the membrane envelope of the virion. The mature S protein comprises two subunits, S1 and S2, generated by post-translational cleavage of a precursor polypeptide. The receptor-binding subunit S1 is variable in sequence and associates closely with the more conserved membrane fusion subunit S2.[26] Intersubunit interactions influence the conformational states and dynamics of both subunits, regulating exposure of the RBDs in S1, their engagement with cellular receptors, and subsequent entry-related rearrangements in S1 and S2 that drive membrane fusion between viral and cellular membranes.[27]

Although a large body of evidence points to a critical role for RBD–receptor interactions in influencing viral host range, findings with multiple coronaviruses also indicate that sequences distal to the RBD–receptor interface, including those at the S1–S2 interface and/or in S2, can impact viral multiplication, virulence, and host-to-host transmission.[18,28–30] For example, D614G, a mutation near the S1–S2 boundary in SARS-CoV-2, is hypothesized to disrupt a salt bridge with K854 in the S2 fusion peptide-proximal region (FPPR).[31] This mutation rapidly increased in frequency and became fixed in the viral population early in the COVID-19 pandemic.[32] The enhanced capacity of mutant D614G spikes to mediate cell entry, with attendant advantages for intra-host viral multiplication and host-to-host transmission, has been proposed as the molecular basis of this selective sweep.[33–35]

Recombinant vesicular stomatitis viruses (rVSVs) encoding coronavirus spike proteins as their only entry glycoprotein have proven useful as biosafety level-2 (BSL-2) surrogates to study viral entry and screen countermeasures. They also afford a safe setting for forward-genetic studies of structure-function relationships in these spikes. Herein, we attempted to generate rVSVs bearing spikes from SHC014-CoV and several other related bat-origin CoVs. Although some of these viruses could be readily recovered from plasmids and propagated in cell culture, others, including rVSV-SHC014 CoV S, were much more challenging to recover, in accordance with previously reported work with single-cycle pseudotypes. Unexpectedly, the successful rescue of rVSV-SHC014 CoV S was associated with the acquisition of a novel point mutation leading to an A835D substitution in the FPPR region of S2 that greatly enhanced entry in the context of both VSV and coronavirus particles. We also identified a second mutation in the N–terminal domain (NTD) of S1 that interacts epistatically with A835D to synergistically increase spike:ACE2 interaction and viral entry. Our findings reveal molecular features that underpin a barrier to cell entry for some bat SL-CoVs and uncover genetic pathways through which this barrier might be overcome by natural selection. They also point to the existence of fitness trade-offs that might alter the evolutionary trajectory of these viruses during host-to-host transmission and identify potential Achilles' heels that could be targeted with countermeasures.

RESULTS

A single point mutation in S2 affords successful rescue of rVSV bearing the SHC014 bat CoV spike.

We sought to generate a panel of replication-competent rVSVs bearing the spikes of bat-origin CoVs as their only entry glycoproteins. We initially selected four sarbecoviruses from clades 1, 2, and 3 with potential for zoonotic transmission in humans—WIV-1, SHC014, RmYN02, and BtKY72.[4,36,37] Previous work has shown that truncations of ≥21 amino acids in the cytoplasmic tails of divergent betacoronavirus spikes enhance the infectivities of VSV and retrovirus surrogates bearing them.[38,39] Accordingly, we replaced the VSV glycoprotein G gene with each CoV S gene engineered to encode a spike protein lacking 21 residues at its C–terminus. We also inserted a sequence encoding the enhanced green fluorescent protein (eGFP) as an independent transcriptional unit at the first position of the VSV genome, as described previously.[40,41]

We attempted to generate each rVSV using a well-established plasmid-based rescue system.[40,42–44] rVSV–WIV-1 S rescued readily, consistent with previous work using coronavirus reverse genetics and describing WIV-1's capacity to use ACE2 from a wide variety of hosts, including humans, civets, and Chinese horseshoe bats.[4] By contrast, numerous attempts failed to yield rVSVs for RmYN02 and BtKY72 (Fig. 1a). rVSV-SHC014-CoV S was similarly challenging to generate; however, a single experiment yielded a replicating viral stock. Nanopore DNA sequencing of an RT-PCR product derived from this viral population revealed that a single point mutation that results in an A835D substitution (corresponding to position 852 in the SARS-CoV-2 spike) in the spike protein, had reached fixation in the population (Supplementary File 1). Sanger sequencing confirmed the presence of A835D as the only mutation in all six plaques isolated from this population. Importantly, a VSV cDNA clone bearing SHC014-CoV S(A835D) was successfully recovered in each of five attempts, whereas its WT counterpart was not (Fig. 1a–b), providing evidence that A835D drives the generation and propagation of rVSV-SHC014-CoV S.

Cognate mutations facilitate the rescue of rVSVs bearing spikes from divergent bat sarbecoviruses.

Amino acid sequence alignment of SHC014-CoV S with those of divergent coronavirus spikes indicated that residue 835 is in the FPPR of S2 (Fig. 1c). The FPPR forms part of an intersubunit interface that is largely buried in the pre-fusion trimer, is highly conserved, and is proposed to play a key role in regulating spike conformation.[45] Most of the betacoronavirus spike sequences we examined, including all sarbecoviruses, bore an Ala at the corresponding residue (Fig. 1c). Accordingly, we postulated that a substitution cognate to A835D in the FPPR of other bat-origin CoV spikes could also enhance entry in the rVSV backbone. Consistent with this hypothesis, we could recover rVSV-RmYN02-CoV S(A806D) and rVSV-BtKY72-CoV S(A837D), even as their WT counterparts failed to rescue (Fig. 1a). Thus, the effect of this amino acid substitution in the spike FPPR appears generalizable to multiple bat CoVs, at least in the genetic and structural context of spikes belonging to the sarbecovirus subgenus.

Figure 1

a

rVSV-CoV S	Genotype	Rescue attempts	Successful rescues
SHC014	WT	10	1*
SHC014	A835D	5	5
RmYN02	WT	9	0
RmYN02	A806D	1	1
BtKY72	WT	9	0
BtKY72	A837D	1	1
WIV1	WT	1	1
WIV1	A835D	1	1

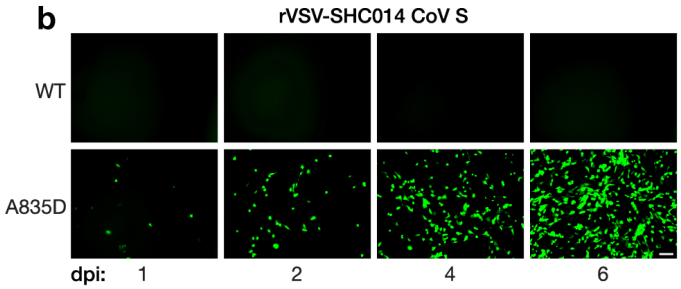

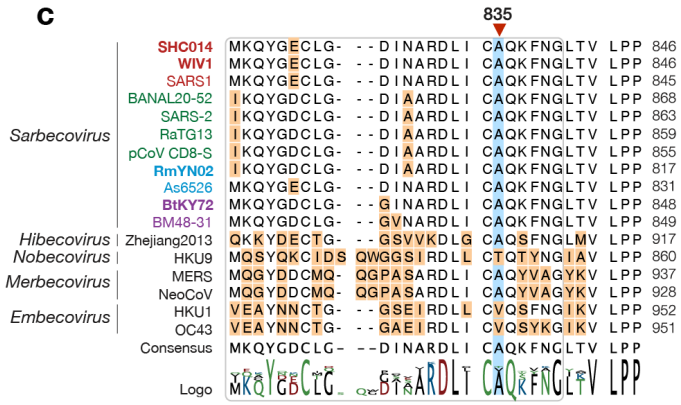

Figure 1 - SHC014 S A835D allows for rVSV rescue and is conserved amongst sarbecoviruses. (a) Summary of recovery attempts of rVSVs bearing SHC014-CoV spike proteins. Asterisk refers to rescue that yielded the A835D substitution. **(b)** Supernatants from 293FT cells co-transfected with plasmids encoding for VSV genomes expressing eGFP and WT or A835D variants of SHC014-CoV spike as well as helper plasmids, were used to infect Vero cells. Representative images show eGFP expression in Vero cells at indicated time points (days post-infection [dpi]). Scale bar, 100 µm. **(c)** Alignment of amino acid sequences in the FPPR region (rounded rectangle) for selected coronavirus spike proteins. Subgenera are indicated in italics. Sarbecoviruses are color-coded by clade (1a: SARS-CoV–like, red; 1b: SARS-CoV-2–like, green; 2: Southeast Asian bat-origin CoV, blue; 3: non-Asian bat-origin CoV, purple). Spikes investigated in the current study are in bold.

A835D greatly enhances the infectivity of authentic coronavirus-like vectors.

We next evaluated the possibility that A835D arose as a spike adaptation specific to the 21-amino acid cytoplasmic tail truncation and/or the heterologous VSV context. To investigate this, we used a recently developed SARS-CoV-2 replicon-based system to generate and evaluate single-cycle replicon-delivery particles (RDPs) trans-complemented with full-length WT or A835D SHC014-CoV spikes.[46] We also generated single-cycle VSV pseudotypes (scVSV) bearing WT or A835D SHC014-CoV spikes, as described previously.[41,47] We compared the infectivities of the VSV (Fig. 2a) and RDP (Fig. 2b) preparations in DBT-9 murine astrocytoma cells previously shown to be ACE2-null and engineered to ectopically express human and intermediate horseshoe bat (*Rhinolophus affinis*) orthologs of ACE2 (*Hs*ACE2 and *Ra*ACE2, respectively).[12,48] Neither the VSVs nor the RDPs could transduce the parental ACE2-null DBT-9 cells, indicating that they require ACE2. This is consistent with previous findings that the SHC014-CoV spike recognizes ACE2 from humans, civets, and horseshoe bats and uses them as entry receptors.[13,20] However, ACE2 overexpression also had little effect on cell entry by both VSVs and RDPs bearing the SHC014-CoV(WT) spike. By contrast, the SHC014-CoV(A835D) spike mediated dose-dependent increases in viral entry, particularly in the cells expressing human and horseshoe bat ACE2 (Fig. 2). Further, rVSV-WIV-1 S(A835D) also exhibited enhanced ACE2-dependent entry relative to WT (Fig. S1). We conclude that the infection-enhancing activity of the A835D mutation is autonomous to the spike protein for multiple sarbecoviruses and can be generalized to authentic CoV virions bearing full-length spikes.

A835D does not alter spike expression or VSV incorporation.

We postulated that the A835D substitution acts in part by increasing the cellular expression and viral incorporation of the SHC014-CoV spike. To test this hypothesis, we transfected 293T cells with plasmid expression vectors encoding the WT and A835D spikes. We observed similar levels of WT and A835D full-length spikes, both in total and at the cell surface (Fig. S2a), indicating that A835D does not enhance SHC014-CoV spike protein expression or steady-state plasma membrane localization. Despite this, scVSVs bearing the A835D spike were much more infectious than their WT counterparts in Vero cells, recapitulating the phenotypes observed in the rVSV and CoV RDP systems (Fig. S2b).

We next used an ELISA to directly assess spike incorporation into viral particles. Specifically, scVSV-coated plates were probed with antibodies specific for the SARS-CoV-2 spike and the VSV internal matrix protein, M, and the Spike-to-M ratio was used as a measure of the relative incorporation of spike into virions. A835D had little or no effect in this assay (Fig. S2c). Taken together, these findings suggest that A835D exerts its effects at a post-assembly step in the viral life cycle, likely during cell entry.

Figure 2

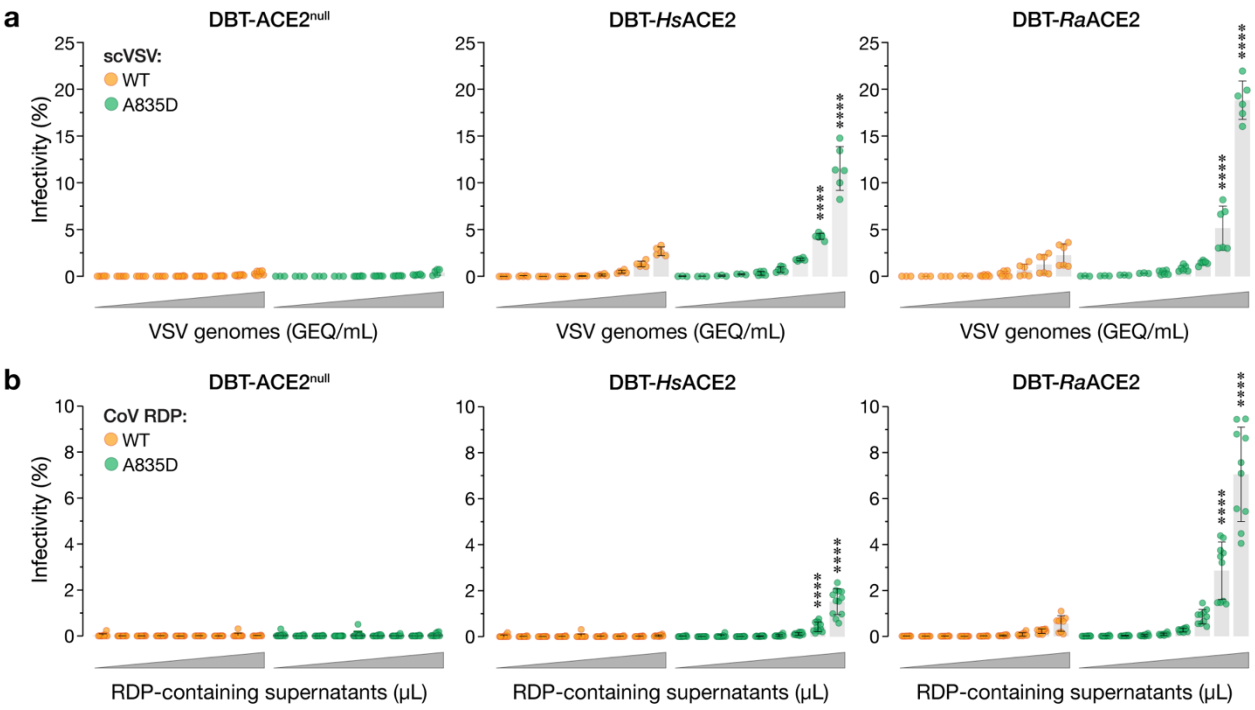

Figure 2 - A835D increases infectivity of cells in an ACE2-dependent manner. (a) Parental DBT-9 cells or DBT-9 cells overexpressing *Hs*ACE2 or *Ra*ACE2 were infected with pre-titrated amounts of scVSV-SHC014 WT or scVSV-SHC014 A835D. Infection was scored by eGFP expression at 16-18 hours post-infection (average±SD, n=5-8 from 3 independent experiments). A range of 7.2×10^2 to 4.5×10^6 viral genome-equivalents (GEQ) was used. **(b)** Parental DBT-9 cells or DBT-9 cells overexpressing *Hs*ACE2 or *Ra*ACE2 were infected with CoV RDPs bearing WT or A835D SHC014-CoV spikes. Infection was scored by mNeonGreen expression at 16-18 hours post-infection (average±SD, n=10-12 from 4-5 independent experiments). Ranges of 8.2×10^3 to 1.8×10^7 GEQ for WT and 6.1×10^3 to 4.0×10^7 for A835D were used. Groups (WT vs. mutant for each cell line) were compared with Welch's t-test with Holm-Šídák correction for multiple comparisons. ns $p>0.05$; ** $p<0.01$; *** $p<0.001$; **** $p<0.0001$. Only the statistically significant comparisons are shown.

A835D enhances SHC014-CoV spike:ACE2 binding.

The preceding findings in cell lines overexpressing ACE2 suggested that A835D acts at least in part by enhancing the capacity of the SHC014-CoV spike to use ACE2 for cell entry. Accordingly, we considered the possibility that, despite its location at a distance from the RBD, A835D may nonetheless augment spike:ACE2 recognition. To test this hypothesis, we first evaluated the capacity of *Hs*ACE2 to capture scVSV-SHC014-CoV S particles in an ELISA. Soluble *Hs*ACE2-coated plates were incubated with genome-normalized amounts of scVSVs,

and particle capture was detected with a CoV spike-specific monoclonal antibody (mAb). Despite previous evidence that the isolated SHC014-CoV spike RBD recognizes *Hs*ACE2 with high avidity,[20] WT SHC014-CoV spike could capture *Hs*ACE2 only poorly, whereas its A835D counterpart exhibited a dramatic, dose-dependent increase in *Hs*ACE2 capture (Fig. 3a).

We next deployed an established biolayer interferometry (BLI) assay to measure binding of the WT and A835D spikes to *Hs*ACE2. Because the A835D substitution is not located in the receptor-binding motif, the binding response can be used as a proxy for RBD exposure or 'availability' to bind ACE2, as shown previously.[49] We began by producing trimeric ectodomains of both spike proteins with a C–terminal T4 fibritin (foldon) domain as described previously for other spikes.[50] Then, equimolar amounts of purified, recombinant SHC014-CoV spike ectodomains were loaded onto BLI probes using an anti-foldon IgG and subsequently dipped into solutions containing *Hs*ACE2. A SARS-CoV-2 spike stabilized with six prolines (Hexapro) served as a positive control and efficiently captured *Hs*ACE2 from solution, as expected.[51] In contrast, WT SHC014-CoV spike bound weakly to *Hs*ACE2, and its activity was substantially boosted by the A835D substitution, corroborating our ELISA results (Fig. 3b-c). Together, these findings strongly suggest that the A835D substitution enhances the SHC014-CoV spike's ability to bind *Hs*ACE2 by increasing the availability of its RBDs for receptor engagement.

Figure 3

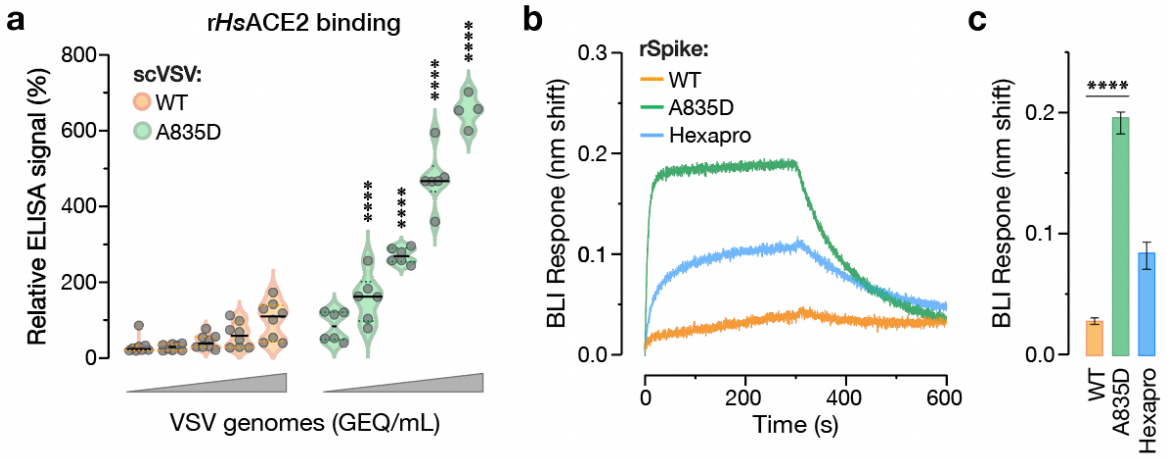

Figure 3 - A835D increases SHC014 S binding to *HsACE2*. (a) Genome-normalized amounts of scVSV particles bearing WT or A835D SHC014 spike were diluted with serial 3-fold dilutions and loaded on an ELISA plate precoated with soluble *Hs*ACE2 and detected with a spike-specific mAb followed by an anti-human HRP-conjugated secondary antibody (average±SD, n=6-8 from 3-4 independent experiments). A range of 1.6×10^6 to 1.3×10^8 viral GEQ was used. Groups (WT vs. mutant) were compared with Welch's t-test with Holm-Šídák correction for multiple comparisons. ns $p>0.05$; ** $p<0.01$; *** $p<0.001$; **** $p<0.0001$. **(b)** Sensorgrams of SHC014-CoV variant spikes and a pre-fusion SARS-CoV-2 spike stabilized with 6 proline substitutions (HexaPro) binding to *Hs*ACE2 by BLI. Similar response levels of spike were

captured using an anti-T4 fibritin (foldon) antibody bound to BLI biosensors and subsequently dipped into wells containing 0.5 μM *Hs*ACE2. Traces of only one replicate of three are shown for clarity. **(c)** Graph of BLI binding response collected in triplicate for the indicated SHC014-CoV spike variants (average±SD). WT and A835D were compared by one-way ANOVA, with Dunnett's correction for multiple comparisons. ns $p>0.05$; ** $p<0.01$; *** $p<0.001$; **** $p<0.0001$. Only the statistically significant comparisons are shown.

High-resolution structure of a SHC014-CoV spike ectodomain.

We performed cryo-electron microscopy (cryo-EM) studies to define the interactions made by residue 835 in the WT SHC014-CoV spike. Purified, soluble spike ectodomain was applied to a cryo-EM grid and vitrified. Sufficient particle density with little aggregation was observed, and a dataset containing 2,025 micrographs was collected (Table S1). Extracted particles were subjected to two-dimensional (2D) classification, which resulted in class averages populated with fully closed trimers, wherein all three RBDs are in the 'down' position. This finding stands in contrast to previous cryo-EM studies of SARS-CoV-2 spike ectodomains, in which substantial proportions of partially open spikes with at least one RBD in the 'up' position were observed.[52–54] A 3.1-Å–resolution 3D reconstruction of the WT SHC014-CoV spike trimer was obtained and found to resemble that of the closed SARS-CoV-2 spike (Figs. 4a, S3 and S4), which was expected given the ≈80% sequence identity between the proteins. The flexibility of the NTD led to poorly resolved regions of the map for this domain, preventing the modeling of some loops based on our reconstruction. Additionally, the FP was not visible in our cryo-EM map, as also observed in many SARS-CoV-2 spike structures. In all, we were able to build residues 33-1124, excluding 45–4, 71–78, 94–97, 121–123, 134–155, 167–182, 205–212, 237–251, 268–270, 617–621, 665–671, and 812-831. Fortunately, C–terminal FPPR residues were resolved (residues 832–840), affording an examination of residue A835 and its local environment.

A835 is part of an α-helix proximal to the FP, and it lies at the interface between protomers (buried surface area upon oligomerization: 22.7%). The A835 sidechain is pointed inward toward V946 in the S2 heptad repeat 1 (HR1) of the same protomer and residues D555, V556 and S557 in the S1 subdomain I (SD1) of the neighboring protomer (corresponding to residues I569 and V963 in the SARS-CoV-2 spike, respectively) (Fig. 4b). Residues 555–557 in SD1 connect A835 to the RBD in the neighboring protomer (Fig. 4d). Structure-based *in silico* analyses consistently suggested that A835D mutation increases the binding free energy between protomers, substantially affecting the stability of the trimer ($\Delta\Delta G_{trimer}$: > 3 Kcal/mol; $\Delta\Delta G_{interface}$: +1.25 Kcal/mol by FoldX; +1.08 Kcal/mol by flexddG). We propose that the introduction of a negatively charged residue at position 835 decreases the stability of the spike trimer by disrupting a network of hydrophobic interactions within (A835–V963) and between protomers (A835–V556; Fig 4b) and triggering unfavorable electrostatic interactions between protomers by virtue of its close proximity to an electronegative surface region in the neighboring protomer (Fig 4c). In support of this hypothesis, scVSVs bearing a Glu at position 835 (A835E) showed a similar enhancement of infectivity over WT as A835D (Fig. S5). Further evidence for the reduced stability of the A835D spike includes a decrease in the expression of its ectodomain relative to WT (Fig. S6a). Moreover, the A835D spike ectodomain was found to be unstable on

cryo-EM grids with mostly dissociated particles and few trimeric spikes, thereby preventing high-resolution structure determination (Fig. S6b-c). Together, these results strongly suggest that the A835D substitution has a destabilizing effect on the pre-fusion conformation of the SHC014-CoV spike, resulting in increased transition of RBDs from ‘down’ to ‘up’ positions and enhanced ACE2 binding.

Figure 4

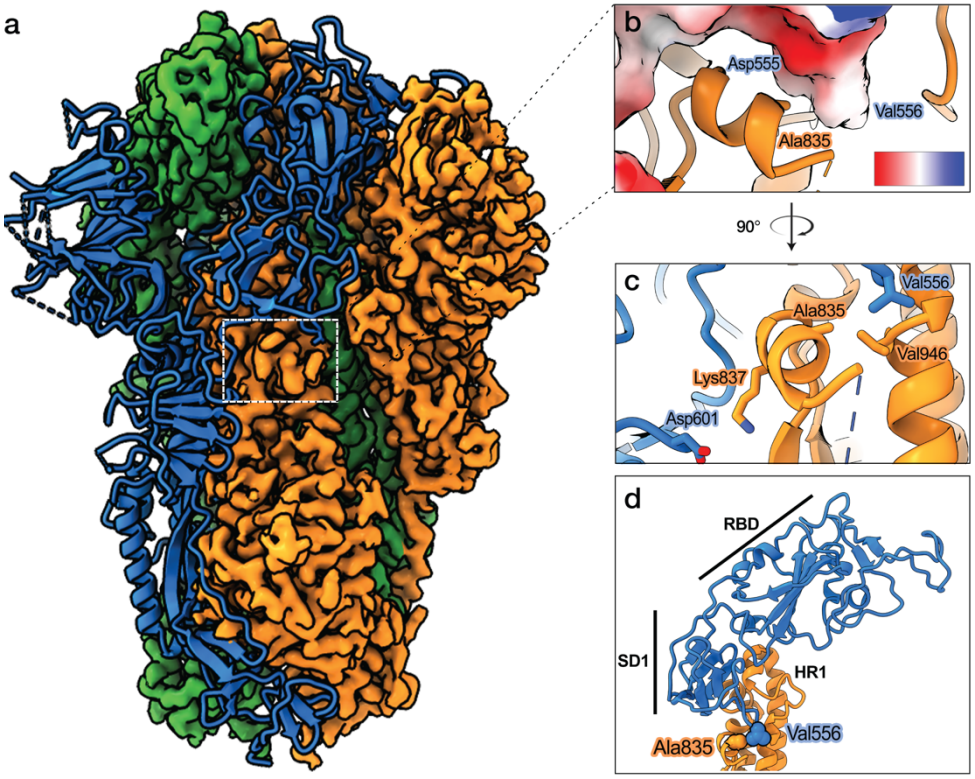

Figure 4 - Structural determination of SHC014-CoV spike. (a) Cryo-EM map and model of the WT SHC014-CoV spike. The cryo-EM map is shown for two protomers and the third protomer is shown as a ribbon representation. **(b)** Ala835 is proximal to Asp555 of the neighboring protomer, which is colored by electrostatic surface potential, red (negative) to blue (positive). Scale bar, -10 to +10 kT/e. **(c)** Ala835 makes van der Waals interactions with Val556 of a neighboring protomer (blue) and Val946 of the same protomer (orange). Lys837 (orange) makes a salt bridge with Asp601 of a neighboring protomer (blue). **(d)** S2 of one protomer (orange) and subdomain 1 (SD1) and RBD of an adjacent protomer (both in blue) are shown as ribbons to depict the distance between the Ala835-containing hydrophobic pocket to the RBD of the adjacent protomer. Labelled residues are shown as spheres.

A835D reduces spike thermostability and alters the temperature dependence of RBD availability.

To test the hypothesis that A835D destabilizes the SHC014-CoV spike, we measured the temperature dependence of viral infectivity loss (inactivation) as a surrogate for the thermal stability of the viral membrane-embedded pre-fusion spike, as we described previously for VSVs bearing filovirus glycoproteins.[55] scVSV particles bearing WT and A835D SHC014-CoV spikes were preincubated at different temperatures, then shifted to 4˚C, and titrated for infectivity on DBT-*Ra*ACE2 cells. WT spike-containing particles suffered loss of infectivity between 48.5–51˚C, with no detectable infectivity at 53˚C. We observed a left shift in temperature-dependent infectivity loss for A835D—the mutant particles underwent inactivation between 41–46˚C, with no detectable infectivity at 48.5˚C (Fig. 5a). Thus, the A835D mutation renders the SHC014-CoV spike more susceptible to thermal inactivation in the context of intact viral particles.

In parallel experiments, we measured the activity of scVSVs bearing WT and A835D SHC014-CoV spikes in the *Hs*ACE2 capture ELISA as a function of temperature. We observed an increase in spike:ACE2 binding for WT particles between 43.5–48˚C, a temperature range just below and overlapping that of viral inactivation for infection. Strikingly, A835D particles exhibited higher levels of *Hs*ACE2 binding at all temperatures tested, with an increase that titrated between 41–43.5˚C, consistent with their temperature range for inactivation (Fig. 5b). We conclude that the A835D mutation has a destabilizing effect on the pre-fusion conformation of the SHC014-CoV spike, sensitizing it to undergo conformational changes in response to heat that result in enhanced RBD exposure and culminate in viral inactivation. We surmise that this phenotype, together with data in Fig. 4 and 5, reflects the increased propensity of the A835D spike to sample open conformers with RBDs in the ‘up’ position at physiological temperatures (see below).

Figure 5

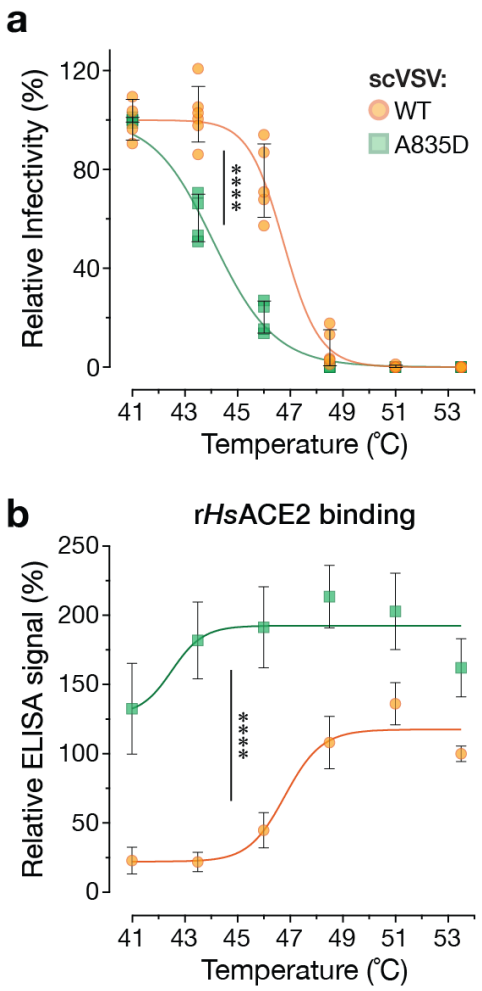

Figure 5 - A835D reduces thermostability of the SHC014-CoV spike. (a) scVSV-SHC014-CoV S particles were incubated at various temperatures for 1 h and used to infect DBT-9 cells overexpressing *Ra*ACE2. Infection levels were normalized to values observed at 41°C for each virus. (average±SD, n=4-6 from 2-3 independent experiments). Area under the curve (AUC) values were calculated for each curve, and groups were compared by one-way ANOVA with Dunnett's correction for multiple comparisons. **(b)** Pre-titrated amounts of scVSV-SHC014-CoV S particles were incubated at various temperatures for 1h and loaded onto *Hs*ACE2-coated ELISA plates. A spike-specific mAb and anti-human HRP-conjugated secondary antibody were used to detect the spike protein. Absorbance values were normalized to that observed for WT particles at 53.5°C. 9.2×10^6 viral GEQs per well were used. (average±SD, n=12 from 6 independent experiments). Groups were compared by two-way ANOVA with Tukey's correction for multiple comparisons, ns $p>0.05$; ** $p<0.01$; *** $p<0.001$; **** $p<0.0001$.

NTD mutation F294L enhances viral entry and ACE2 recognition by WT spike but its effect is much greater on the A835D spike.

In seeking to identify key intra-spike interactions altered by the A835D mutation while structural studies on the SHC014-CoV spike (Fig. 4) were in progress, we modeled both WT and A835D SHC014-CoV spikes using AlphaFold2.[56,57] These studies suggested that A835D may engage in a new polar interaction with residue T842 in the FPPR. Although we could not structurally corroborate this hypothesis given the relative instability of the A835D ectodomain, we nonetheless attempted to generate an rVSV bearing an SHC014-CoV(A835D/T842A) double-mutant spike. As with the WT spike, the double mutant was challenging to rescue, but one attempt yielded a replicating viral population. Nanopore sequencing of viral cDNA from this population indicated that both parental mutations were present but uncovered one additional point mutation in the spike NTD, F294L (corresponding to position F306 in the SARS-CoV-2 spike), in most reads (Supplementary File 2). Sanger sequencing confirmed the acquisition of F294L and retention of both parental mutations in all three plaques isolated from this population, strongly suggesting that F294L played a functional role in rVSV recovery.

To test this hypothesis, we sought to examine the effect of F294L alone as well as in combination with A835D, since F294L was originally selected in the A835D background. Accordingly, we attempted to rescue rVSVs with SHC014-CoV(F294L) and SHC014-CoV(F294L+A835D) spikes in parallel with rVSV-SHC014-CoV A835D and WT spikes as controls. Rescues of rVSV-SHC014 bearing spikes with F294L, A835D, and F294L+A835D were all successful, with F294L+A835D rescuing the fastest, followed by A835D, and then F294L (Fig. 6a). As we observed previously (Fig. 1b), WT did not rescue. Sanger sequencing of the spike gene in isolated plaques confirmed the presence of only these mutations in each respective virus prep.

Next, we generated scVSVs bearing WT and mutant SHC014-CoV spikes. Spikes containing F294L alone exhibited increases relative to WT in cell entry (Fig. 6b) and *Hs*ACE2 binding (Fig. 7a) resembling those observed for A835D. F294L+A835D conferred a striking additive enhancement in infectivity relative to the single mutants in DBT-9 cells over-expressing *Hs*ACE2 and *Ra*ACE2 (Fig. 6b), corroborating our findings in the rVSV rescue experiments (Fig. 6a). These boosts in infectivity were also associated with a commensurate, dramatic gain in *Hs*ACE2 binding to viral particles at 37˚C (Fig. 7a). BLI analyses of *Hs*ACE2 binding to SHC014-CoV spike ectodomains bearing F294L and F294L+A835D yielded largely concordant results, but with some differences (Fig. 7b). Specifically, although F294L did significantly enhance spike:*Hs*ACE2 binding, its effect was smaller than that observed for A835D. Further, F294L+A835D did not boost *Hs*ACE2 binding over A835D alone. These discordances between the virus- and spike ectodomain-based ACE2 binding assays may simply reflect the greater instability of the ectodomains bearing A835D relative to viral membrane-embedded spikes—juxtamembrane and transmembrane sequences in the latter are predicted to counteract the destabilizing effects of the ectodomain mutations.[58–60] Alternatively, or in addition, they may reflect total saturation of the BLI biosensors, preventing further increases in RBD availability from being measured. We conclude that F294L and A835D independently enhance ACE2 recognition and spike-dependent entry but synergize when combined to afford viral particles a selective advantage in entry over the single mutants.

Figure 6

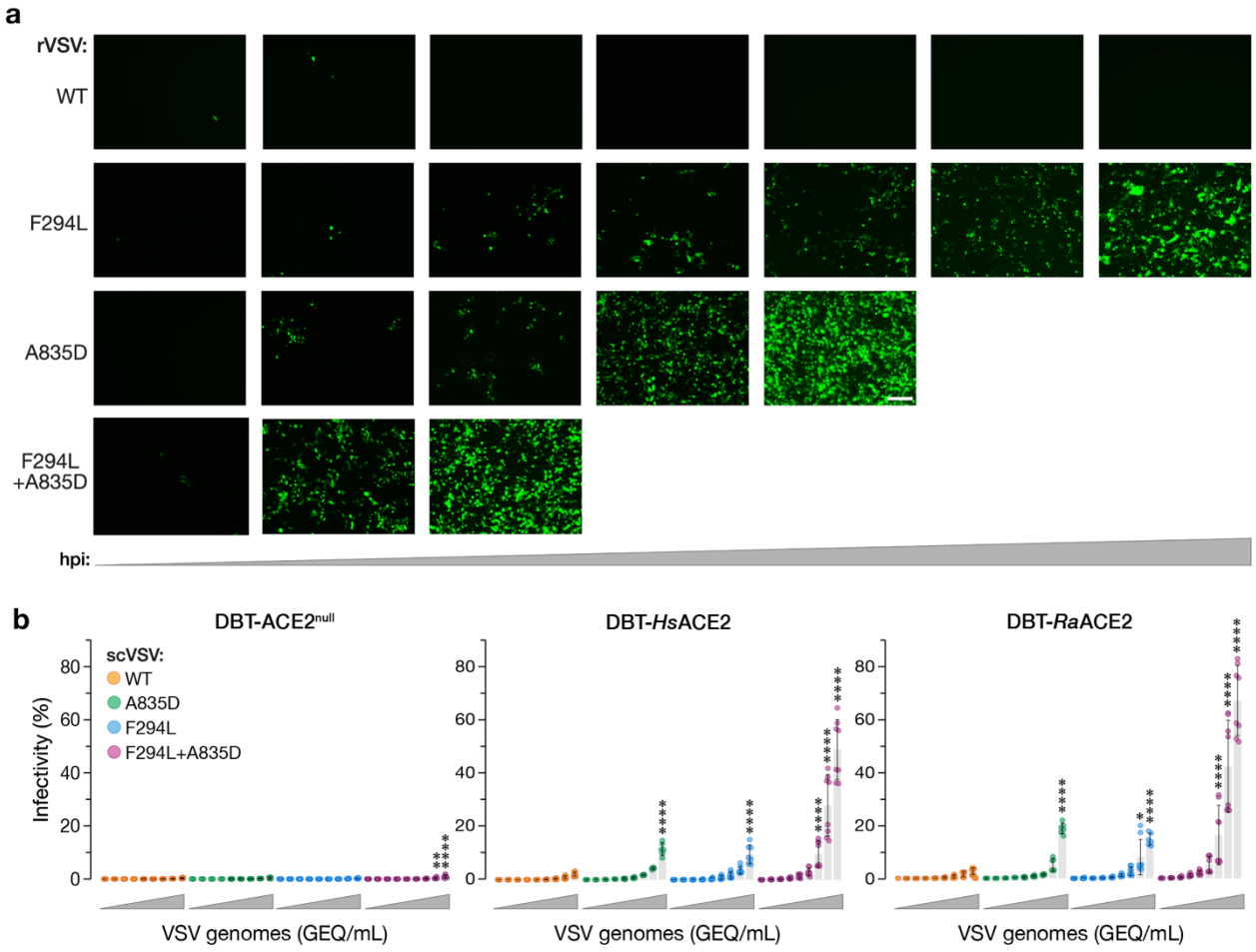

Figure 6 – A835D and F294L substitutions synergize to enhance infectivity. (a) Supernatants from 293FT cells co-transfected with plasmids encoding for VSV genomes expressing eGFP and WT, A835D, F294L, or F294L+A835D variants of SHC014-CoV spike as well as helper plasmids, were used to infect Vero cells. Representative images show eGFP expression in Vero cells at 24, 60, 108, 204, 252, 276, and 273 h post-infection [hpi]. Representative images are shown. Scale bar, 100 µm. **(b)** Parental DBT-9 cells or DBT-9 cells overexpressing *Hs*ACE2 or *Ra*ACE2 were infected with pre-titrated amounts of scVSV-SHC014 particles bearing WT, A835D, F294L, or F294L+A835D spike. Infection was scored by eGFP expression at 16–18 hours post-infection (average±SD, n=5-8 from 3 independent experiments). A range of 1.5×10^3 to 9.6×10^6 viral GEQ was used. Groups (WT vs. mutant for each cell line) were compared with Welch's t-test with Holm-Šídák correction for multiple comparisons. ns $p>0.05$; ** $p<0.01$; *** $p<0.001$; **** $p<0.0001$. Only the statistically significant comparisons are shown.

F294L and A835D act through distinct mechanisms.

The location of F294L in the NTD, at a substantial distance from the receptor-binding motif, indicated that its effect on spike:*Hs*ACE2 binding is indirect, and as with A835D, likely mediated by a change in the RBD availability of pre-fusion spikes. To begin to uncover F294L's mechanism of action and the basis of its synergism with A835D, we investigated its effects on spike thermal stability in both the WT and A835D contexts. As described above (Fig. 5a), scVSV particles bearing each spike were preincubated at different temperatures and then titrated for infectivity on DBT-*Ra*ACE2 cells (Fig. 7c). Unlike with A835D, we observed little or no left shift in the temperature dependence of thermal inactivation for F294L alone, relative to WT. Moreover, the F294L+A835D double mutant resembled its A835D parent in thermal stability, sharing a large left shift in thermal inactivation, as observed in Fig. 5a (Fig. 7c). Therefore, F294L does not contribute to spike destabilization, which is concordant with our observation that the F294L spike ectodomain resembles its WT counterpart in expression level and pre-fusion stability. Expression levels were compared by overlaying absorbance traces from size-exclusion chromatography (SEC) of different variants. All cultures were prepared in parallel in a similar manner, allowing for direct comparison (Fig. S6a).

Finally, we examined the capacity of F294L to alter RBD availability in a temperature-dependent manner by *Hs*ACE2 capture ELISA (Fig. 7d). Consistent with its behavior in the thermal inactivation studies (Fig. 7c), F294L afforded an increase in *Hs*ACE2 binding that titrated over a similar temperature range as WT. Strikingly, however, the F294L+A835D double mutant exhibited a large increase in *Hs*ACE2 binding at all temperatures tested, with no discernible temperature-dependent effect between 37–55˚C. We conclude that F294L enhances RBD availability via a mechanism distinct from that of A835D. Taken together, our findings raise the possibility that the changes in spike structure and dynamics elicited by A835D enhance F294L's mode of action, thereby creating mechanistic synergy between these mutations (see Discussion). This synergy affords a substantial increase in RBD availability at physiological temperature and thus, the enhanced infectivity of the double mutant relative to WT and its single-mutant counterparts.

RBD-mobilizing substitutions enhance viral sensitivity to antibody neutralization.

Previous work with SARS-CoV-2 variants of concern has shown that amino acid substitutions which modulate spike dynamics can alter the exposure of neutralizing antibody epitopes.[61–63] The large increases in RBD availability mediated by A835D and F294L suggested that these mutations might also impact viral susceptibility to antibody neutralization. To investigate this possibility, we measured the activity of Adagio-2 (ADG2), a broad neutralizer of clade 1 sarbecoviruses, which binds an RBD epitope accessible only in the 'up' RBD[64,65] against VSVs bearing WT and mutant SHC014-CoV spikes. We observed little neutralization of WT at mAb concentrations as high as 500 nM. In contrast, A835D, F294L, and A835D+F294L spikes were all neutralized by ADG2 with sensitivities proportional to their capacity to recognize ACE2 (Fig. 7a) and mediate entry (A835D+F294L > A835D > F294L) (Fig. 6b). Remarkably, incorporation of both mutations into the SHC014-CoV spike afforded an enhancement in neutralization IC_{50} of >500-fold (Fig. 7e). These findings provide additional evidence that A835D and F294L enhance viral entry by increasing RBD exposure. Moreover, they suggest that mutations of this type would be subject to a substantial fitness tradeoff in the form of enhanced

sensitivity to neutralizing antibodies, with likely implications for their evolutionary trajectories during adaptation to new hosts following zoonotic transmission.

Figure 7

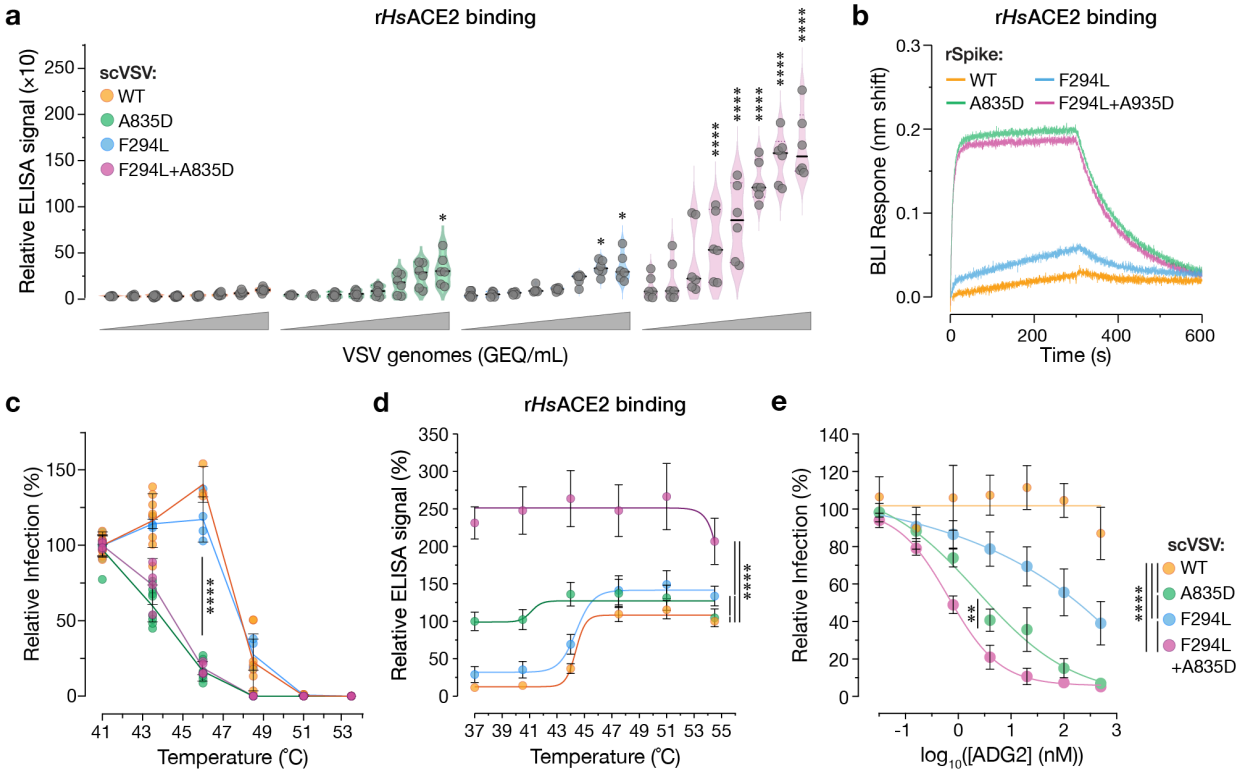

Figure 7 – A835D and F294L synergize to enhance ACE2 binding but act through distinct mechanisms. (a) Genome normalized amounts of scVSV particles bearing WT, A835D, F294L, or F294L+A835D SHC014-CoV spike were diluted with serial 3-fold dilutions and loaded on an ELISA plate precoated with soluble *Hs*ACE2 and detected with a spike-specific mAb followed by an anti-human HRP-conjugated secondary antibody (average±SD, n=6-8 from 3-4 independent experiments). A range of 5.5×10^3 to 1.2×10^7 viral GEQ was used. Groups (WT vs. mutant) were compared with Welch's t-test with Holm-Šídák correction for multiple comparisons. ns p>0.05; ** p<0.01; *** p<0.001; **** p<0.0001. **(b)** Sensorgrams of SHC014-CoV spike variants binding to *Hs*ACE2 by BLI. Spike variants were captured to similar response levels using an anti-T4 fibritin antibody bound to BLI biosensors and subsequently dipped into wells containing 0.5 μM *Hs*ACE2. One of three replicates is shown for clarity. **(c)** scVSV-SHC014-CoV S particles were incubated at various temperatures for 1h and used to infect DBT-9 cells overexpressing *Ra*ACE2. Infection levels were normalized to values observed at 41°C for each virus (average±95%CI, n=4-8 from 2-4 independent experiments). AUC values were calculated for each curve, and groups were compared by one-way ANOVA with Dunnett's correction for multiple comparisons. Statistical significance is shown for WT vs. A835D, WT vs. F294L+A835D, F294L vs. A835D, and F294L vs. F294L+A835D. Differences among all other two-way comparisons were not statistically significant **(d)** Pre-titrated amounts of scVSV-

SHC014-CoV S particles were incubated at various temperatures for 1 h and loaded onto *Hs*ACE2-coated ELISA plates. A spike-specific mAb and anti-human HRP-conjugated secondary antibody were used to detect the spike protein. Absorbance values were normalized to that observed for WT particles at 54.5°C. (average±95%CI, n=12 from 3 independent experiments). 5.1×10^6 viral GEQs were used per well. AUC values were calculated for each curve, and groups were compared by one-way ANOVA with Dunnett's correction for multiple comparisons. **(e)** Pre-titrated amounts of scVSV-SHC014-CoV S bearing WT, A835D, F294L, or F294L+A835D spikes were incubated with serial 3-fold dilutions of mAb ADG-2 starting at 500 nM, at 37°C for 1 h. Virus:mAb mixtures were applied to monolayers of Vero cells. At 18 h post-infection, cells were fixed, nuclei were counterstained, and infected cells were scored by eGFP expression (average±SD, n=9 from 3 independent experiments). AUC values were calculated for each curve, and groups were compared by one-way ANOVA with Dunnett's post hoc test, ns $p>0.05$; ** $p<0.01$; *** $p<0.001$; **** $p<0.0001$. Only the statistically significant comparisons are shown.

DISCUSSION

Bat-origin CoVs with high sequence similarity to their human outbreak-causing counterparts pose continuing risks to human populations. Consequently, considerable effort has been expended in understanding their biology and uncovering the molecular determinants of their spillover potential. Because few authentic CoVs isolated from nature or recovered from molecular clones are available, and generating and working with these agents requires a high biosafety setting, researchers have largely turned to surrogate systems, including single-cycle pseudotyped viruses and recombinant proteins, to study 'pre-emergent' CoV spike proteins. Herein, we systematically exploited the forward-genetic capabilities of rVSVs to investigate molecular adaptation in a panel of these spikes. We found that the successful recovery and high replicative fitness of rVSVs bearing WT spikes from SHC014-CoV was associated with the acquisition of two growth-adaptive amino acid substitutions outside the RBD. Through studies with both viral particles and recombinant spike proteins, we show that these substitutions synergistically enhance viral receptor binding and entry by regulating spike conformation, even though they are spatially separated in the three-dimensional structure of the SHC014-CoV spike (also determined herein). Our findings confirm the importance of interactions among the S1 NTD and RBD and the S2 FPPR sequences in the CoV spike in influencing virus-receptor interactions and entry[66] but also highlight the existence of distinct, context-dependent, and at least partially transferable genetic pathways for viral adaptation in the non-RBD spike sequences of bat-origin CoVs, including a positive intramolecular epistasis that alters intersubunit interactions. Similar pathways may be accessible to bat-origin CoVs during spillover and sustained host-to-host transmission. Further, they may provide diagnostic markers useful for evaluating the potential for emergence, expansion, and transmissibility of zoonotic strains associated with sporadic human cases.

Recent work suggests that, in contrast to SARS-CoV-2, multiple pre-fusion spikes from CoVs of rhinolophid bat and pangolin origin (e.g., BANAL-20-52, BANAL-20-236, RaTG13, Pangolin-CoV), have evolved to favor a more compact 'closed' state, wherein their RBDs largely

sample the 'down' conformation that is incompetent for receptor binding.[17,67,68] Nonetheless, spikes derived from these viruses could associate with ACE2 and mediate entry into cells expressing human and rhinolophid ACE2 orthologs, indicating that their RBDs can infrequently transit to the 'up' conformation and engage ACE2. Our structural studies on an ectodomain of the WT SHC014-CoV spike also revealed only closed trimers with all three RBDs in the down position on the EM grids. In contrast to these previous findings, however, we found that the SHC014-CoV spike bound weakly with *Hs*ACE2 and was ineffective at viral entry into cells expressing human or rhinolophid ACE2 in both VSV and CoV contexts. Together with previous observations that the isolated SHC014-CoV spike RBD binds to diverse ACE2 orthologs with high affinity,[20] these findings suggested that the availability of receptor-accessible 'up' RBDs is even lower in SHC014-CoV (and likely, also in RmYN02-CoV and BtkY72-CoV, the other bat-origin CoVs examined herein). Although somewhat surprising, these results are consistent with previous observations by Menachery and colleagues that lentiviral SHC014-CoV pseudotypes have little activity in human ACE2-expressing cells.[13] Moreover, in at least one instance in which SHC014-CoV S pseudotypes were employed as part of larger CoV spike panels, they were found to have ~10-fold lower titers in *Hs*ACE2-overexpressing cells relative to their WIV-1–CoV counterparts; A. Balazs, personal communication). The totality of the evidence thus supports the conclusion that, although the pre-fusion spikes of many bat-origin CoVs tend to favor the closed (all RBDs down) state, they exist along a continuum with regard to their propensity to sample conformationally open states that are competent to bind receptors.

We identified a key genetic adaptation for successful rVSV-SHC014-CoV S rescue and multiplication—mutation A835D in the S2 FPPR. In accordance with our structural and biochemical findings, this mutation boosted cell entry through substantial enhancements in human and rhinolophid ACE2 binding in both viral particle- and ectodomain-based assays. Studies on SARS-CoV-2 have highlighted the influence of a disulfide-bonded helix-turn-helix–forming sequence in the FPPR on spike conformational dynamics and RBD positioning.[45,69] Specifically, structures of full-length spikes suggested that, in its ordered state, the FPPR clamps the RBD in its 'down' position and stabilizes the closed conformation of the spike trimer. A structural transition in the FPPR from ordered to disordered, possibly favored at endosomal acidic pH, was proposed to initiate a conformational relay that repositions the RBD to the 'up' state and drives spike opening.[66] A C–terminal segment of the FPPR was ordered in our high-resolution cryo-EM structure of the WT SHC014-CoV spike, and we anticipate that A835D would disrupt a network of intra- and inter-protomer hydrophobic interactions with residues in the S1 CTD and S2 heptad repeat 1 (HR1) and trigger unfavorable electrostatic interactions between protomers, thereby affording greater movement of the FPPR and leading to increased RBD availability.

Through rVSV rescue experiments in an A835D mutant background, we identified a second entry-enhancing mutation, F294L, in the NTD of the SHC014-CoV spike. Although F294L, like A835D, could act alone by increasing RBD availability, combining the two mutations afforded substantial, synergistic increases in both viral infectivity and RBD availability. Strikingly, F294L did not reduce spike thermostability, which we conjecture may be incompatible with assembly of the pre-fusion spike in the context of the already destabilizing A835D. In the WT spike, F294 is located near the C–terminus of the NTD (Fig. S7b), and is coordinated by contacts with K266 and K288 in the adjacent NTD-RBD linker to form a 'double-cation-pi'

sandwich (Fig. S7a). We propose that the loss of this interaction network in the F294L spike enhances the flexibility of the NTD-RBD linker—implicated in S1 inter-domain movements in the SARS-CoV-2 spike— thereby increasing RBD availability.[70] Although more work is needed to uncover the molecular basis of F294L+A835D synergy, we posit that interactions among the NTD, RBD, and FPPR sequences substantially limit the mobility of the NTD-RBD linker in the WT SHC014-CoV spike. Disruption of RBD-FPPR interaction in the A835D mutant is predicted to free the linker to contribute to the RBD movements associated with spike opening. The inherently more mobile NTD-RBD linker in F294L may allow even larger inter-domain movements in the context of the more open A835D spike, mediating a synergistic increase in RBD availability.

We conclude that F294L and A835D form a positive intramolecular epistasis, a phenomenon in which the combined effect of two or more mutations in a protein is greater than (and/or distinct from) the sum of their individual effects. Multiple examples of epistasis have been documented for the SARS-CoV-2 spike, and some are proposed to play crucial roles in shaping viral evolution over the course of the COVID-19 pandemic. Especially notable are specific substitutions that appear key in modulating the effects of suites of other mutations on spike cleavage, stability, and/or opening (D614G and H655Y),[71] receptor binding (e.g., N501Y),[72] and/or neutralizing antibody escape (e.g., E484K),[61,73,74] and whose acquisition may therefore have driven pronounced shifts in the adaptive trajectories of viral lineages. Herein, we found that engineering of mutations cognate to A835D in the bat-origin CoV spikes of RmYN02 (clade 2) and BtKY72 (clade 3) afforded the rescue of rVSVs bearing these spikes, suggesting that the spike-opening effect of this mutation is transferable to divergent sarbecovirus genetic backgrounds. Since BtKY72 requires ACE2[20,75] whereas RmYN02 does not,[36] this effect appears independent of receptor usage. A835D also enhanced the efficiency of the highly entry-competent WIV-1 spike (Fig. S1), implying that it can function in the distinct genetic background of WIV-1, which affords a relatively open pre-fusion spike despite its A835/F294 genotype. Interestingly, although A835 is highly conserved among sarbecovirus spikes, the residue cognate to 294 is already polymorphic (F/L) (Fig. S7c), raising the possibility that the acquisition of new mutations in different 294 backgrounds could promote epistatic shifts in viral fitness.

Observations that the pre-fusion spikes of many bat-origin CoVs,[16] as well as the four human endemic CoVs,[50,76–79] predominantly assume a closed conformation in structural studies may reflect a requirement for viral replication in immune-competent hosts with pre-existing antiviral immunity. We speculate that, in bat-origin CoVs with especially stable spikes (such as SHC014-CoV), this phenomenon may also be coupled with viral adaptation to a fecal-oral transmission lifestyle in the insectivorous bat host. To wit, Ou and co-workers recently found that an entry-enhancing mutation in Laotian sarbecoviruses proposed to increase spike opening rendered viral particles more susceptible to proteolytic inactivation.[17] These authors postulated that repeated viral passage through the highly proteolytic environment of the gut may have selected for spike stability at the expense of entry efficiency. Conversely, a body of work has shown that exogenous treatment with the gut serine protease trypsin can activate many CoV spikes with monobasic S1-S2 and S2′ cleavage sites, a process that likely resembles spike activation in the gut of the natural hosts.[5,19,80–82] Given the known interplay between spike cleavage, conformational dynamics, and fusion triggering,[34,67,70,83] it is thus conceivable that the extreme stability of the SHC014-CoV spike reflects a setpoint that is tuned for its activation to

bind its receptor and undergo fusion triggering in the protease-rich milieu of the gut lumen. This setpoint would also be expected to reduce viral exposure to immune surveillance (see below).

Current evidence raises the possibility that such spike optimizations for replication in the natural host impose a barrier to viral transmission via the respiratory route,[19,81,84,85] at least in part because the virus must adapt to use the host proteases enriched in the respiratory tract, such as the plasma membrane serine protease TMPRSS2,[86,87] instead of luminal gut proteases. Indeed, recent work indicates that clade 2 sarbecoviruses, in particular, require treatment with exogenous trypsin to infect cells.[5,19,80,88] We speculate that this behavior at least partly reflects a high degree of spike stability, similar to our findings herein with SHC014-CoV. A distinct strategy exemplified by divergent coronaviruses, most notably SARS-CoV-2[89] and MERS-CoV[90], is the acquisition of a furin cleavage site at the S1-S2 boundary, which not only affords spike cleavage in virus-producer cells,[91,92] but also appears to enhance TMPRSS2-mediated SARS-CoV-2 spike cleavage in target cells.[93] The SARS-CoV-2 spike furin site promotes viral entry and respiratory transmission in a ferret model[94] but also destabilizes its pre-fusion conformation, likely causing the selection of D614G as a stabilizing compensatory mutation.[34,95] We posit that the novel spike-opening epistasis between S2 and S1 mutations uncovered in the current study represents yet another conceivable path for spike adaptation to a proteolytically poor environment—one that does not require spike pre-cleavage in producer cells. Finally, we cannot currently exclude the possibility that A835D+F294L also directly enhances spike cleavage(s) and/or downstream steps, such as S1 shedding, in the conformational cascade leading to membrane fusion. Mutations in the spikes of SARS-CoV-2 and other bat-origin CoVs that contribute to spike opening (e.g., T372A in the RBD)[16,17,96] at the expense of stability may also act in a manner similar to A835D+F294L to drive viral entry.

A limitation of the experimental evolution ‘sandbox’ we have explored herein is its relative simplicity—viral clones in our cell culture system would have encountered only a small subset of the competitive pressures faced by their counterparts in the wild. Crucial among these countervailing pressures are those imposed by the host immune system. As a case in point, mutations in bat-origin CoV spikes that engender a more open spike architecture might be more vulnerable to antibody neutralization due to enhanced epitope exposure, as shown for the T372A RBD mutant in SARS-CoV-2.[17] In line with this hypothesis, we found that the WT SHC014-CoV spike was almost completely resistant to neutralization by an RBD-directed antibody, whereas the mutants were highly sensitive. To our knowledge, these dramatic shifts in neutralization susceptibility are much greater than any reported to date, and they attest to both the extremely closed nature of the WT SHC014-CoV spike and the degree to which the entry-enhancing mutations reported in this study afford spike opening. Mutants of the type described herein may therefore suffer a considerable fitness cost in a physiological context. However, they may also provide an advantageous genetic background upon which to accrue additional mutations that maximize fitness by balancing spike stability, entry efficiency, and susceptibility to antibody neutralization during zoonotic adaptation of bat-origin CoVs.

ACKNOWLEDGMENTS

We thank Ralph S. Baric for his provision of DBT-9–based cell lines and suggestions on a preliminary version of this manuscript. This work was supported by grant INV-031624 from the Bill & Melinda Gates Foundation (to K.C. and J.S.M) and the National Institutes of Health (R01AI132633 to K.C., P01AI165075 to C.M.R.). C.M.R. was additionally supported by the Meyer Foundation, the BAWD Foundation, The G. Harold and Leila Y. Mathers Charitable Foundation, and Fast Grants (www.fastgrants.org). J.S.M. was additionally supported by Welch Foundation grant number F-0003-19620604. AL.T. and J.B. were additionally supported by the NIH training grants T32GM007288 (Medical Scientist Training Program) and T32AI070117 (Geographic Medicine and Emerging Infections), respectively, at Albert Einstein College of Medicine. E.H.M. was additionally supported by the Institute for Clinical and Translational Research at Einstein and Montefiore (K12TR004411). I.R.L. was supported by a Bulgari Women & Science fellowship. RKJ was partly supported by NIH grants (P20GM134974 and R21AI156482). T.B. is supported by the A.G. Leventis Foundation, Shurl and Kay Curci Foundation, and Thermo Fisher Scientific Antibody Fellowships.

COMPETING INTERESTS

KC is a member of the scientific advisory board and holds shares in Integrum Scientific, LLC. KC is a cofounder of and holds shares in Eitr Biologics Inc. I.R.L. and C.M.R. are inventors on a patent describing SARS-CoV-2 replicons filed by The Rockefeller University.

AUTHOR CONTRIBUTIONS

Conceptualization: ALT, CMA, REA, RKJ, JSM, KC, EHM
Methodology: ALT, CMA, IRL, JB, GL, REA, CMR, RKJ, JSM, KC, EHM
Investigation: ALT, CMA, IRL, JB, GL, TB, FLK, LC, GLM, AMC, CL, RKJ, EHM
Writing—Original Draft: ALT, CMA, GL, JSM, KC, EHM
Writing—Review & Editing: All authors
Visualization: ALT, CMA, GL, JSM, KC, EHM
Supervision: REA, CMR, JSM, KC, EHM

METHODS

Cell Lines

293FT cells (Thermo Fisher) were cultured in high-glucose Dulbecco's Modified Eagle Medium (DMEM, Thermo Fisher) supplemented with 10% fetal bovine serum (FBS, Gemini), 1% Glutamax (Thermo Fisher), and 1% penicillin-streptomycin (P/S, Thermo Fisher). African green monkey kidney Vero Cells (ATCC) were cultured in high-glucose DMEM supplemented with 2% FBS, 1% Glutamax, and 1% P/S. Embryonic kidney fibroblast 293T cells (ATCC) were cultured in DMEM supplemented with 10% FBS, 1% Glutamax, and 1% P/S.

DBT-9 cells (gift of Ralph Baric, source unknown) [97,98] were cultured in Minimum Essential Medium α (MEMα, Thermo Fisher) supplemented with 10% FBS, 1% Glutamax, 1% P/S, and 1% Amphotericin (Thermo Fisher). Cells overexpressing ACE2 were also cultured with 5ug/mL puromycin (Gibco).

These cell lines were subcultured every 2–3 days using 0.05% Trypsin/EDTA (Gibco). All cell lines were maintained in a humidified 37°C incubator supplied with 5% CO2.

Plasmids

Plasmids encoding human codon-optimized spike (S) of SHC014 (GenBank accession number KC881005.1), WIV-1 (GenBank accession number KC881007), BtKY72 (GenBank accession number KY352407), and RmYN02 (GenBank accession number MW201982) in the VSV genome with an eGFP gene, were generated as previously described.[40,41,43,44,99]

Sarbecovirus sequence alignment

Sequence alignment of amino acid sequences of the fusion peptide proximal region (FPPR) of the S protein of selected sarbecoviruses were aligned using CLUSTAL Omega.[100]

Generation of recombinant VSVs

A plasmid encoding the VSV genome was modified to replace its glycoprotein, G, with the wild-type or mutant spike glycoprotein gene of SHC014, WIV-1, BtKY72, or RmYN02 with a 21-amino acid C-tail truncation. The VSV genome also encodes for an eGFP reporter gene as a separate transcriptional unit. Replication-competent, recombinant VSVs (rVSVs) bearing these S proteins were generated via a plasmid-based rescue system in 293FT cells as previously described.[40,41,43,44,99] Briefly, 293FT cells were transfected with the VSV plasmid and plasmids expressing T7 polymerase and VSV N, P, M, G, and L proteins using polyethylenimine. Forty-eight hours post transfection, supernatants from the transfected cells were transferred to Vero cells. Viral growth was monitored by an eGFP reporter every day. Viral stocks were plaque purified on Vero cells. Spike sequences were amplified from viral genomic RNA by RT-PCR and analyzed by Sanger sequencing and/or minION sequencing.

Generation of pseudotyped VSVs

Single cycle VSV pseudotypes bearing SHC014 S proteins and an eGFP reporter, were produced in 293T cells as described previously.[101,102] Briefly, 293T cells were transfected with a

plasmid encoding an expression vector and the SHC014 S. Two days later, cells were infected with a passage stock of VSVG/ΔG for 1h at 37°C. Cells were washed eight times with high glucose media to remove any residual VSV-G. Viral supernatant was harvested two days later and pelleted by ultracentrifugation.

Generation of replication-competent delivery particles (RDPs)
Single-cycle SARS-CoV2 RDPs bearing WT or mutant SHC014 spikes were generated as described previously.[46] Briefly, BHK-21 cells were transfected with plasmids encoding the full-length WT or mutant SHC014 spikes. The following day, cells were electroporated with ΔSpike nsp1- SARS-CoV2-mNeonGreen replicon RNA and N mRNA. 24h post electroporation, the RDP-containing supernatants were collected and filtered through a 0.4µM filter to remove cell debris.

SHC014-CoV Spike Glycoprotein Ectodomain Expression and Purification
Amino acids 1-1191 of SHC014-CoV spike were coupled to a C–terminal foldon motif, 3C protease site, 8X histidine tag, and Twin-Strep tag and cloned into a pαH vector. For variants, substitutions F294L and A835D were incorporated into this background. All variants were expressed by polyethylenimine-induced transient transfection of FreeStyle 293-F cells (Thermo Fisher). After 6 days, the cell supernatants were harvested by centrifugation and clarified via passage through a 0.22 µm filter. Variants were purified from filtered supernatant via gravity flow over StrepTactin resin (IBA) followed by gel-filtration chromatography on a Superose 6 10/300 column (GE Healthcare) into a buffer consisting of 2 mM Tris pH 8.0, 200 mM NaCl, 0.02% NaN_3.

***HsACE2* Expression and Purification**
Amino acids 1-615 of HsACE2 were coupled to a PreScission site, 8X histidine tag, and Strep Tag II and cloned into a pαH vector. HsACE2 was expressed by polyethylenimine-induced transient transfection of FreeStyle 293-F cells (Thermo Fisher). After 6 days, the cell supernatant was harvested by centrifugation and clarified via passage through a 0.22 µm filter. *Hs*ACE2 was then purified from filtered supernatant via gravity flow over StrepTactin XT resin (IBA) followed by gel-filtration chromatography on a Superdex 200 Increase 10/300 column (GE Healthcare) into a buffer consisting of 2 mM Tris pH 8.0, 200 mM NaCl, 0.02% NaN_3.

Method Details

Nanopore sequencing
Viral RNA was isolated from rescue population supernatants (Zymogen Quick-RNA viral Kit). cDNA was then generated through reverse transcription (Invitrogen Superscript III). PCR reactions were performed to amplify the cDNA population (NEB Q5 Hotstart). Following this Oxford Nanopore, MinION long read DNA sequencing was performed to identify mutations present in the viral population. Sequenced bases were called by Guppy (https://community.nanoporetech.com/docs/prepare/library_prep_protocols/Guppy-protocol/v/gpb_2003_v1_revax_14dec2018/guppy-software-overview) and the resulting sequences were assembled using the de novo assembly tool Shasta (https://github.com/chanzuckerberg/shasta/blob/master/docs/ComputationalMethods.html). The

resulting assembled contigs were aligned to the reference genome utilizing Smith-Waterman local alignments.

Detection of SHC014-CoV spike surface expression

293FT cells were seeded in six-well plates. 24 hours later, cells were transfected with 2ug of expression plasmids encoding either nothing, SHC014 S WT, or A835D, and 1ug of a plasmid encoding for RFP. 24 hours post transfection, cells were blocked with 0.5% bovine serum albumin (BSA, Sigma Aldrich) in PBS for 30 minutes at 4°C. SHC014 S was stained by a spike-specific mAb, ADG-2 (20ug/mL) followed by anti-human Alexa Fluor 488 (4ug/mL) for 1 hour at 4°C each. After extensive washing, stained cells were filtered through a 41-µm nylon net filter (Millipore) and analyzed using a BD FACSCalibur Flow Cytometer and FlowJo software.

Detection of SHC014-CoV spike total expression

293FT cells were seeded in six-well plates. 24 hours later, cells were transfected with 2ug of expression plasmids encoding either nothing, SHC014 S WT, or A835D, and 1ug of a plasmid encoding for RFP. 24 hours post transfection, cells were collected at fixed with 4% formaldehyde at room temperature (RT) for 5 minutes. Cells were washed and permeabilized with 1X permeabilization buffer (Tonbo Biosciences) for 15 minutes at RT. Cells were blocked with 10% FBS in permeabilization buffer for 30 minutes at RT. Following washing, cells were stained with ADG-2 (20ug/mL) followed by anti-human Alexa Fluor 488 (4ug/mL). After extensive washing, stained cells were filtered through a 41-µm nylon net filter (Millipore) and analyzed using a BD FACSCalibur Flow Cytometer and FlowJo software.

ELISA for detection of scVSV-SHC014-CoV S binding to soluble *HsACE2*

High-protein binding 96-well ELISA plates (Corning) were coated with 2ug/mL of soluble HsACE2 overnight at 4°C. Plates were then washed with PBS and blocked with PBS containing 3% BSA for 1h at 37°C. Blocked plates were exposed to scVSV-SHC014-CoV, in duplicate, at pre-titrated amounts that were diluted in a 3-fold serial dilution, for 1 hour at 37°C. Plates were washed with PBS and incubated with 10nM of ADG-2 for 1h at 37°C. Following washing, anti-human IgG secondary antibody conjugated to horseradish peroxidase was added for 1h at 37°C. Plates were washed, 1-Step™ Ultra TMB-ELISA Substrate Solution (Thermo Fisher) was added and quenched with the addition of 2 M sulfuric acid. Absorbance was read at 450 nm.

Biolayer interferometry (BLI)

An IgG targeting T4 fibritin (foldon) was immobilized to anti-human Fc (AHC) Octet biosensors (FortéBio) to a response level of 1.0 nm. Tips were then submerged into solutions of SHC014-CoV spike variants in 20 mM Tris pH 8.0, 150 mM NaCl, 1 mg/mL bovine serum albumin, and 0.01% Tween-20, capturing variants to similar response levels. Spike-bound biosensors were subsequently dipped into 500 nM HsACEII in 20 mM Tris pH 8.0, 150 mM NaCl, 1 mg/mL bovine serum albumin, and 0.01% Tween-20 [103] to observe receptor association. Dissociation of HsACEII was then observed by submersion into a buffer consisting of 20 mM Tris pH 8.0, 150 mM NaCl, 1 mg/mL bovine serum albumin, and 0.01% Tween-20. The relative proportion of accessible RBDs was quantified as previously described.[103] Data were collected in triplicate.

Cryo-EM Data Collection

The SHC014-CoV S ectodomain data set was collected on a Thermo Scientific Glacios operating at 200 kV utilizing a Falcon 4 direct electron detector. C-Flat 1.2/1.3 grids (Electron Microscopy Sciences) were glow discharged at 20 mA for 30 seconds. Samples were prepared by application of 4 uL of a 1.0 mg/mL solution of spike onto grids. Grids were then blotted for 4 seconds using a blot force of -3 and a wait time of 5 seconds on a Vitrobot Mark IV (Thermo Scientific) set to 100% humidity at room temperature. The blotted grid was subsequently plunge-frozen into liquid ethane. All data were collected at 150,000x magnification, which gave a pixel size of 0.94 Å. In total, 2,025 exposures were taken using a defocus range of -1 to -2 microns, an exposure time of 13.2 seconds, and a total electron exposure of ~50 $e^-/Å^2$. Data were collected using SerialEM.

Cryo-EM Data Processing

The cryo-EM data were pre-processed using cryoSPARC Live v3[104] for motion correction and patch CTF estimation. Exposures were subsequently transferred to cryoSPARC v3 for manual curation, blob particle picking, particle extraction, and 2D classification. 1,653 exposures were accepted after curation, which resulted in 649,312 particle picks. After 2D classification, 150,716 particles remained and were used in a 4-class *ab initio* reconstruction job. The four output volumes were used with all particles for heterogeneous refinement. The best class contained 79,540 particles, which was used for homogenous refinement with both C1 and C3 symmetry, leading to reconstructions at 3.7 Å and 3.2 Å resolution, respectively. A total of 76,442 particles were then subjected to a non-uniform refinement with C3 symmetry, leading to a 3.1 Å resolution reconstruction.

An initial model of the WT SHC014-CoV spike was generated using AlphaFold2[56] and fitting into the 3.1 Å cryo-EM map in ChimeraX.[105,106] The model was subsequently refined iteratively in Isolde,[107] Coot,[108] and Phenix.[109] Structural figures were generated in ChimeraX.

***In silico* Binding Free Energy Calculation Between Spike Protomers**

Optimization of the cryo-EM structure: Missing loops were modeled via various tools including Swiss Model,[110] AlphaFold2,[56] Prime Homology Modeling,[111] and Modeller.[112] Resultant loops were grafted onto the resolved Cryo-EM structure via in-house Visual Molecular Dynamics scripts. Uniprot and comparison to human SARS-CoV-2 spike system structure were used to identify necessary disulfide bonds (15 per monomer). Ectodomain glycosites were predicted and confirmed as described[113,114] Our modeled construct is fully N-/O-glycosylated following a similar human glycoprofile as described,[103] which was consistent with Watanabe and co-workers.[115] Protonation states for all titratable residues were assigned using PROPKA[116] at pH 7.4, and histidine protonation states were assigned with Schrodinger's Protein Preparation Wizard.[117] The resultant SHC014 glycoprotein was parameterized for minimization and short equilibration according to CHARMM36 all-atom additive force fields for proteins and glycans.[118,119] The SHC014 construct was fully solvated with explicit water molecules using the TIP3P model[120] and neutralized with a 150 mM concentration of sodium and chloride ions. The system was then minimized, heated to 310 K, and briefly equilibrated using NAMD3[121] with standard molecular dynamics simulations protocols. For a complete set of grafting, system construction, glycoprofile details, minimization, heating, equilibration scripts, and complete methodological details, please

see all shared scripts and shared model files which will be provided on the AmaroLab website (https://amarolab.ucsd.edu/covid19.php).

Binding free energy calculation (interface ΔΔG): We ran two separate methods (FoldX and flex ddG) to estimate the binding affinity change between interacting protomers in the SCH014 spike trimer.[122,123] Using FoldX, we performed five rounds of internal structure optimization (FoldX repairPDB), and iteratively modeled and assessed A835D (25 iterations; FoldX BuildModel and AnalyseComplex). Flex ddG: calculation parameters were set as follows, nrstruct=35, max_minimization_iter=5000, abs_score_convergence_thresh=1m, number_backrub_trials=35000. In order to make the calculation tractable with flex ddG, we assessed the effect of A835D using a subset of residues (chain A: residues 691 to 1124; chain C: residues 18 to 689). The reported ΔΔG for each method corresponds to the averaged ΔΔG.

Virus Infection Assays

24 hours prior to infection, adherent cells were seeded in high glucose media on 96 well plates (Corning). Vero cells were plated at 2 x 10^4 cells per well. DBT-9 cells were plated at 1.8 x 10^4 cells per well. Prior to infection, virus was diluted in corresponding media and infected cells were incubated at 37°C for 12-18 hours. Cells were then fixed with 4% paraformaldehyde, stained with Hoechst-33342 (Invitrogen) before eGFP+ cells were counted using a Cytation 5 reader (BioTek Instruments). Infection levels were calculated as a percentage of eGFP+ cells over the total number of cells.

Temperature-Dependent Infection Assays

DBT-9 cells overexpressing RsACE2 were seeded 24 hours prior to infection in high glucose media on 96 well plates at 1.8 x 10^4 cells per well. scVSV-SHC014-CoV particles were diluted in PBS and incubated at a temperature range from 37°C to 55°C (actual range per virus indicated in Results) for 1 hour and subsequently placed on ice. After cooling, virus was added to cells and incubated at 37°C for 12-18 hours. Cells were then fixed with 4% paraformaldehyde, stained with Hoechst 33342 (Invitrogen) before eGFP+ cells were counted using a Cytation 5 reader (BioTek Instruments). Infection levels were calculated as a percentage of eGFP+ cells over the total number of cells.

Temperature-Dependent Binding Assays

scVSV-SHC014-CoV particles were diluted in PBS and incubated at a temperature range from 37°C to 55°C (actual range per virus indicated in Results) for 1 hour and subsequently placed on ice. After cooling, virus was added onto high-binding 96-well plates precoated with soluble *HsACE2*. Plates were blocked with 3% BSA in PBS. SHC014 S was detected with ADG-2. Bound antibody was then detected with an anti-human antibody conjugated to HRP. Plates were washed, 1-Step™ Ultra TMB-ELISA Substrate Solution (Thermo Fisher) was added and quenched with the addition of 2 M sulfuric acid, per manufacturer recommendations. Absorbance was read at 450 nm. All binding steps were carried out at 37°C for 1h. Binding curves were generated using Prism (GraphPad Software, La Jolla, CA).

ADG-2 Neutralization Assay

mAb ADG2 was serially diluted and mixed with pre-diluted scVSV-SHC014 WT, A835D, F294L, or F294L A835D in infection media (DMEM, 2% FBS, 1% P/S, 1% Q). Mixtures were incubated for 1 hr at 37°C. Virus/antibody inoculum was added to DBT-*RaACE2* cells, pre-seeded in 96 well plates and incubated for 12-18 hours. Cells were fixed with 4% paraformaldehyde (Sigma), washed with PBS, and stored in PBS containing Hoechst-33342 (Invitrogen) at a dilution of 1:4000. Viral infectivity was measured by automated enumeration of GFP-positive cells from captured images using a Cytation5 automated fluorescence microscope (BioTek) and analyzed using the Gen5 data analysis software (BioTek).

BIBLIOGRAPHY

1. Zhou, H., Ji, J., Chen, X., Bi, Y., Li, J., Wang, Q., Hu, T., Song, H., Zhao, R., Chen, Y., et al. (2021). Identification of novel bat coronaviruses sheds light on the evolutionary origins of SARS-CoV-2 and related viruses. Cell *184*, 4380-4391.e14. 10.1016/j.cell.2021.06.008.

2. Cohen, L.E., Fagre, A.C., Chen, B., Carlson, C.J., and Becker, D.J. (2023). Coronavirus sampling and surveillance in bats from 1996-2019: a systematic review and meta-analysis. Nat. Microbiol. *8*, 1176–1186. 10.1038/s41564-023-01375-1.

3. Temmam, S., Vongphayloth, K., Baquero, E., Munier, S., Bonomi, M., Regnault, B., Douangboubpha, B., Karami, Y., Chrétien, D., Sanamxay, D., et al. (2022). Bat coronaviruses related to SARS-CoV-2 and infectious for human cells. Nature *604*, 330–336. 10.1038/s41586-022-04532-4.

4. Ge, X.-Y., Li, J.-L., Yang, X.-L., Chmura, A.A., Zhu, G., Epstein, J.H., Mazet, J.K., Hu, B., Zhang, W., Peng, C., et al. (2013). Isolation and characterization of a bat SARS-like coronavirus that uses the ACE2 receptor. Nature *503*, 535–538. 10.1038/nature12711.

5. Letko, M., Marzi, A., and Munster, V. (2020). Functional assessment of cell entry and receptor usage for SARS-CoV-2 and other lineage B betacoronaviruses. Nat. Microbiol. *5*, 562–569. 10.1038/s41564-020-0688-y.

6. Lam, T.T.-Y., Jia, N., Zhang, Y.-W., Shum, M.H.-H., Jiang, J.-F., Zhu, H.-C., Tong, Y.-G., Shi, Y.-X., Ni, X.-B., Liao, Y.-S., et al. (2020). Identifying SARS-CoV-2-related coronaviruses in Malayan pangolins. Nature *583*, 282–285. 10.1038/s41586-020-2169-0.

7. Hu, B., Zeng, L.-P., Yang, X.-L., Ge, X.-Y., Zhang, W., Li, B., Xie, J.-Z., Shen, X.-R., Zhang, Y.-Z., Wang, N., et al. (2017). Discovery of a rich gene pool of bat SARS-related coronaviruses provides new insights into the origin of SARS coronavirus. PLoS Pathog. *13*, e1006698. 10.1371/journal.ppat.1006698.

8. Murakami, S., Kitamura, T., Suzuki, J., Sato, R., Aoi, T., Fujii, M., Matsugo, H., Kamiki, H., Ishida, H., Takenaka-Uema, A., et al. (2020). Detection and Characterization of Bat Sarbecovirus Phylogenetically Related to SARS-CoV-2, Japan. Emerging Infect. Dis. *26*, 3025–3029. 10.3201/eid2612.203386.

9. Ren, W., Qu, X., Li, W., Han, Z., Yu, M., Zhou, P., Zhang, S.-Y., Wang, L.-F., Deng, H., and Shi, Z. (2008). Difference in receptor usage between severe acute respiratory syndrome (SARS) coronavirus and SARS-like coronavirus of bat origin. J. Virol. *82*, 1899–1907. 10.1128/JVI.01085-07.

10. Liu, K., Pan, X., Li, L., Yu, F., Zheng, A., Du, P., Han, P., Meng, Y., Zhang, Y., Wu, L., et al. (2021). Binding and molecular basis of the bat coronavirus RaTG13 virus to ACE2 in humans and other species. Cell *184*, 3438-3451.e10. 10.1016/j.cell.2021.05.031.

11. Rockx, B., Sheahan, T., Donaldson, E., Harkema, J., Sims, A., Heise, M., Pickles, R., Cameron, M., Kelvin, D., and Baric, R. (2007). Synthetic reconstruction of zoonotic and early human severe acute respiratory syndrome coronavirus isolates that produce fatal disease in aged mice. J. Virol. *81*, 7410–7423. 10.1128/JVI.00505-07.

12. Sheahan, T., Rockx, B., Donaldson, E., Sims, A., Pickles, R., Corti, D., and Baric, R. (2008). Mechanisms of zoonotic severe acute respiratory syndrome coronavirus host range expansion in human airway epithelium. J. Virol. *82*, 2274–2285. 10.1128/JVI.02041-07.

13. Menachery, V.D., Yount, B.L., Debbink, K., Agnihothram, S., Gralinski, L.E., Plante, J.A., Graham, R.L., Scobey, T., Ge, X.-Y., Donaldson, E.F., et al. (2015). A SARS-like cluster of circulating bat coronaviruses shows potential for human emergence. Nat. Med. *21*, 1508–1513. 10.1038/nm.3985.

14. Menachery, V.D., Yount, B.L., Sims, A.C., Debbink, K., Agnihothram, S.S., Gralinski, L.E., Graham, R.L., Scobey, T., Plante, J.A., Royal, S.R., et al. (2016). SARS-like WIV1-CoV poised for human emergence. Proc Natl Acad Sci USA *113*, 3048–3053. 10.1073/pnas.1517719113.

15. Cantoni, D., Mayora-Neto, M., Thakur, N., Elrefaey, A.M.E., Newman, J., Vishwanath, S., Nadesalingam, A., Chan, A., Smith, P., Castillo-Olivares, J., et al. (2022). Pseudotyped Bat Coronavirus RaTG13 is efficiently neutralised by convalescent sera from SARS-CoV-2 infected patients. Commun. Biol. *5*, 409. 10.1038/s42003-022-03325-9.

16. Zhang, S., Qiao, S., Yu, J., Zeng, J., Shan, S., Tian, L., Lan, J., Zhang, L., and Wang, X. (2021). Bat and pangolin coronavirus spike glycoprotein structures provide insights into SARS-CoV-2 evolution. Nat. Commun. *12*, 1607. 10.1038/s41467-021-21767-3.

17. Ou, X., Xu, G., Li, P., Liu, Y., Zan, F., Liu, P., Hu, J., Lu, X., Dong, S., Zhou, Y., et al. (2023). Host susceptibility and structural and immunological insight of S proteins of two SARS-CoV-2 closely related bat coronaviruses. Cell Discov. *9*, 78. 10.1038/s41421-023-00581-9.

18. Zheng, Y., Shang, J., Yang, Y., Liu, C., Wan, Y., Geng, Q., Wang, M., Baric, R., and Li, F. (2018). Lysosomal proteases are a determinant of coronavirus tropism. J. Virol. *92*. 10.1128/JVI.01504-18.

19. Guo, H., Li, A., Dong, T.-Y., Su, J., Yao, Y.-L., Zhu, Y., Shi, Z.-L., and Letko, M. (2022). ACE2-Independent Bat Sarbecovirus Entry and Replication in Human and Bat Cells. MBio, e0256622. 10.1128/mbio.02566-22.

20. Starr, T.N., Zepeda, S.K., Walls, A.C., Greaney, A.J., Alkhovsky, S., Veesler, D., and Bloom, J.D. (2022). ACE2 binding is an ancestral and evolvable trait of sarbecoviruses. Nature *603*, 913–918. 10.1038/s41586-022-04464-z.

21. Zheng, M., Zhao, X., Zheng, S., Chen, D., Du, P., Li, X., Jiang, D., Guo, J.-T., Zeng, H., and Lin, H. (2020). Bat SARS-Like WIV1 coronavirus uses the ACE2 of multiple animal species as receptor and evades IFITM3 restriction via TMPRSS2 activation of membrane fusion. Emerg. Microbes Infect. *9*, 1567–1579. 10.1080/22221751.2020.1787797.

22. Hauser, B.M., Sangesland, M., St Denis, K.J., Lam, E.C., Case, J.B., Windsor, I.W., Feldman, J., Caradonna, T.M., Kannegieter, T., Diamond, M.S., et al. (2022). Rationally designed immunogens enable immune focusing following SARS-CoV-2 spike imprinting. Cell Rep. *38*, 110561. 10.1016/j.celrep.2022.110561.

23. Halfmann, P.J., Loeffler, K., Duffy, A., Kuroda, M., Yang, J.E., Wright, E.R., Kawaoka, Y., and Kane, R.S. (2024). Broad protection against clade 1 sarbecoviruses after a single immunization with cocktail spike-protein-nanoparticle vaccine. Nat. Commun. *15*, 1284. 10.1038/s41467-024-45495-6.

24. Cohen, A.A., Gnanapragasam, P.N.P., Lee, Y.E., Hoffman, P.R., Ou, S., Kakutani, L.M., Keeffe, J.R., Wu, H.-J., Howarth, M., West, A.P., et al. (2021). Mosaic nanoparticles elicit cross-reactive immune responses to zoonotic coronaviruses in mice. Science *371*, 735–741. 10.1126/science.abf6840.

25. Zhao, X., Qiu, T., Huang, X., Mao, Q., Wang, Y., Qiao, R., Li, J., Mao, T., Wang, Y., Cun, Y., et al. (2024). Potent and broadly neutralizing antibodies against sarbecoviruses induced by sequential COVID-19 vaccination. Cell Discov. *10*, 14. 10.1038/s41421-024-00648-1.

26. Jackson, C.B., Farzan, M., Chen, B., and Choe, H. (2021). Mechanisms of SARS-CoV-2 entry into cells. Nat. Rev. Mol. Cell Biol. *23*, 3–20. 10.1038/s41580-021-00418-x.

27. Huang, Y., Yang, C., Xu, X.-F., Xu, W., and Liu, S.-W. (2020). Structural and functional properties of SARS-CoV-2 spike protein: potential antivirus drug development for COVID-19. Acta Pharmacol. Sin. *41*, 1141–1149. 10.1038/s41401-020-0485-4.

28. Wang, Q., Qi, J., Yuan, Y., Xuan, Y., Han, P., Wan, Y., Ji, W., Li, Y., Wu, Y., Wang, J., et al. (2014). Bat origins of MERS-CoV supported by bat coronavirus HKU4 usage of human receptor CD26. Cell Host Microbe *16*, 328–337. 10.1016/j.chom.2014.08.009.

29. Shang, J., Wan, Y., Luo, C., Ye, G., Geng, Q., Auerbach, A., and Li, F. (2020). Cell entry mechanisms of SARS-CoV-2. Proc Natl Acad Sci USA *117*, 11727–11734. 10.1073/pnas.2003138117.

30. Yang, Y., Du, L., Liu, C., Wang, L., Ma, C., Tang, J., Baric, R.S., Jiang, S., and Li, F. (2014). Receptor usage and cell entry of bat coronavirus HKU4 provide insight into bat-to-human transmission of MERS coronavirus. Proc Natl Acad Sci USA *111*, 12516–12521. 10.1073/pnas.1405889111.

31. Zhang, J., Cai, Y., Xiao, T., Lu, J., Peng, H., Sterling, S.M., Walsh, R.M., Rits-Volloch, S., Zhu, H., Woosley, A.N., et al. (2021). Structural impact on SARS-CoV-2 spike protein by D614G substitution. Science *372*, 525–530. 10.1126/science.abf2303.

32. Yurkovetskiy, L., Wang, X., Pascal, K.E., Tomkins-Tinch, C., Nyalile, T.P., Wang, Y., Baum, A., Diehl, W.E., Dauphin, A., Carbone, C., et al. (2020). Structural and Functional Analysis of the D614G SARS-CoV-2 Spike Protein Variant. Cell *183*, 739-751.e8. 10.1016/j.cell.2020.09.032.

33. Plante, J.A., Liu, Y., Liu, J., Xia, H., Johnson, B.A., Lokugamage, K.G., Zhang, X., Muruato, A.E., Zou, J., Fontes-Garfias, C.R., et al. (2021). Spike mutation D614G alters SARS-CoV-2 fitness. Nature *592*, 116–121. 10.1038/s41586-020-2895-3.

34. Zhang, L., Jackson, C.B., Mou, H., Ojha, A., Peng, H., Quinlan, B.D., Rangarajan, E.S., Pan, A., Vanderheiden, A., Suthar, M.S., et al. (2020). SARS-CoV-2 spike-protein D614G mutation increases virion spike density and infectivity. Nat. Commun. *11*, 6013.

10.1038/s41467-020-19808-4.

35. Hou, Y.J., Chiba, S., Halfmann, P., Ehre, C., Kuroda, M., Dinnon, K.H., Leist, S.R., Schäfer, A., Nakajima, N., Takahashi, K., et al. (2020). SARS-CoV-2 D614G variant exhibits efficient replication ex vivo and transmission in vivo. Science *370*, 1464–1468. 10.1126/science.abe8499.

36. Zhou, H., Chen, X., Hu, T., Li, J., Song, H., Liu, Y., Wang, P., Liu, D., Yang, J., Holmes, E.C., et al. (2020). A Novel Bat Coronavirus Closely Related to SARS-CoV-2 Contains Natural Insertions at the S1/S2 Cleavage Site of the Spike Protein. Curr. Biol. *30*, 2196-2203.e3. 10.1016/j.cub.2020.05.023.

37. Tao, Y., and Tong, S. (2019). Complete Genome Sequence of a Severe Acute Respiratory Syndrome-Related Coronavirus from Kenyan Bats. Microbiol. Resour. Announc. *8*. 10.1128/MRA.00548-19.

38. Dieterle, M.E., Haslwanter, D., Bortz, R.H., Wirchnianski, A.S., Lasso, G., Vergnolle, O., Abbasi, S.A., Fels, J.M., Laudermilch, E., Florez, C., et al. (2020). A Replication-Competent Vesicular Stomatitis Virus for Studies of SARS-CoV-2 Spike-Mediated Cell Entry and Its Inhibition. Cell Host Microbe *28*, 486-496.e6. 10.1016/j.chom.2020.06.020.

39. Yu, J., Li, Z., He, X., Gebre, M.S., Bondzie, E.A., Wan, H., Jacob-Dolan, C., Martinez, D.R., Nkolola, J.P., Baric, R.S., et al. (2021). Deletion of the SARS-CoV-2 Spike Cytoplasmic Tail Increases Infectivity in Pseudovirus Neutralization Assays. J. Virol. *95*. 10.1128/JVI.00044-21.

40. Wong, A.C., Sandesara, R.G., Mulherkar, N., Whelan, S.P., and Chandran, K. (2010). A forward genetic strategy reveals destabilizing mutations in the Ebolavirus glycoprotein that alter its protease dependence during cell entry. J. Virol. *84*, 163–175. 10.1128/JVI.01832-09.

41. Slough, M.M., Chandran, K., and Jangra, R.K. (2019). Two point mutations in old world hantavirus glycoproteins afford the generation of highly infectious recombinant vesicular stomatitis virus vectors. MBio *10*. 10.1128/mBio.02372-18.

42. Whelan, S.P., Ball, L.A., Barr, J.N., and Wertz, G.T. (1995). Efficient recovery of infectious vesicular stomatitis virus entirely from cDNA clones. Proc Natl Acad Sci USA *92*, 8388–8392. 10.1073/pnas.92.18.8388.

43. Kleinfelter, L.M., Jangra, R.K., Jae, L.T., Herbert, A.S., Mittler, E., Stiles, K.M., Wirchnianski, A.S., Kielian, M., Brummelkamp, T.R., Dye, J.M., et al. (2015). Haploid genetic screen reveals a profound and direct dependence on cholesterol for hantavirus membrane fusion. MBio *6*, e00801. 10.1128/mBio.00801-15.

44. Jangra, R.K., Herbert, A.S., Li, R., Jae, L.T., Kleinfelter, L.M., Slough, M.M., Barker, S.L., Guardado-Calvo, P., Román-Sosa, G., Dieterle, M.E., et al. (2018). Protocadherin-1 is essential for cell entry by New World hantaviruses. Nature *563*, 559–563. 10.1038/s41586-018-0702-1.

45. Cai, Y., Zhang, J., Xiao, T., Peng, H., Sterling, S.M., Walsh, R.M., Rawson, S., Rits-Volloch, S., and Chen, B. (2020). Distinct conformational states of SARS-CoV-2 spike

protein. Science *369*, 1586–1592. 10.1126/science.abd4251.

46. Ricardo-Lax, I., Luna, J.M., Thao, T.T.N., Le Pen, J., Yu, Y., Hoffmann, H.-H., Schneider, W.M., Razooky, B.S., Fernandez-Martinez, J., Schmidt, F., et al. (2021). Replication and single-cycle delivery of SARS-CoV-2 replicons. Science *374*, 1099–1106. 10.1126/science.abj8430.

47. Farzani, T.A., Chov, A., and Herschhorn, A. (2020). A protocol for displaying viral envelope glycoproteins on the surface of vesicular stomatitis viruses. STAR Protocols *1*, 100209. 10.1016/j.xpro.2020.100209.

48. Hou, Y.J., Chiba, S., Leist, S.R., Meganck, R.M., Martinez, D.R., Schäfer, A., Catanzaro, N.J., Sontake, V., West, A., Edwards, C.E., et al. (2023). Host range, transmissibility and antigenicity of a pangolin coronavirus. Nat. Microbiol. *8*, 1820–1833. 10.1038/s41564-023-01476-x.

49. Sztain, T., Ahn, S.-H., Bogetti, A.T., Casalino, L., Goldsmith, J.A., Seitz, E., McCool, R.S., Kearns, F.L., Acosta-Reyes, F., Maji, S., et al. (2021). A glycan gate controls opening of the SARS-CoV-2 spike protein. Nat. Chem. *13*, 963–968. 10.1038/s41557-021-00758-3.

50. Kirchdoerfer, R.N., Cottrell, C.A., Wang, N., Pallesen, J., Yassine, H.M., Turner, H.L., Corbett, K.S., Graham, B.S., McLellan, J.S., and Ward, A.B. (2016). Pre-fusion structure of a human coronavirus spike protein. Nature *531*, 118–121. 10.1038/nature17200.

51. Hsieh, C.-L., Goldsmith, J.A., Schaub, J.M., DiVenere, A.M., Kuo, H.-C., Javanmardi, K., Le, K.C., Wrapp, D., Lee, A.G., Liu, Y., et al. (2020). Structure-based design of prefusion-stabilized SARS-CoV-2 spikes. Science *369*, 1501–1505. 10.1126/science.abd0826.

52. Wrapp, D., Wang, N., Corbett, K.S., Goldsmith, J.A., Hsieh, C.-L., Abiona, O., Graham, B.S., and McLellan, J.S. (2020). Cryo-EM structure of the 2019-nCoV spike in the prefusion conformation. Science *367*, 1260–1263. 10.1126/science.abb2507.

53. Ke, Z., Oton, J., Qu, K., Cortese, M., Zila, V., McKeane, L., Nakane, T., Zivanov, J., Neufeldt, C.J., Cerikan, B., et al. (2020). Structures and distributions of SARS-CoV-2 spike proteins on intact virions. Nature *588*, 498–502. 10.1038/s41586-020-2665-2.

54. Walls, A.C., Park, Y.-J., Tortorici, M.A., Wall, A., McGuire, A.T., and Veesler, D. (2020). Structure, Function, and Antigenicity of the SARS-CoV-2 Spike Glycoprotein. Cell *181*, 281-292.e6. 10.1016/j.cell.2020.02.058.

55. Bortz, R.H., Wong, A.C., Grodus, M.G., Recht, H.S., Pulanco, M.C., Lasso, G., Anthony, S.J., Mittler, E., Jangra, R.K., and Chandran, K. (2020). A Virion-Based Assay for Glycoprotein Thermostability Reveals Key Determinants of Filovirus Entry and Its Inhibition. J. Virol. *94*. 10.1128/JVI.00336-20.

56. Jumper, J., Evans, R., Pritzel, A., Green, T., Figurnov, M., Ronneberger, O., Tunyasuvunakool, K., Bates, R., Žídek, A., Potapenko, A., et al. (2021). Highly accurate protein structure prediction with AlphaFold. Nature *596*, 583–589. 10.1038/s41586-021-03819-2.

57. Gutnik, D., Evseev, P., Miroshnikov, K., and Shneider, M. (2023). Using alphafold predictions in viral research. Curr. Issues Mol. Biol. *45*, 3705–3732.

10.3390/cimb45040240.

58. Broer, R., Boson, B., Spaan, W., Cosset, F.-L., and Corver, J. (2006). Important role for the transmembrane domain of severe acute respiratory syndrome coronavirus spike protein during entry. J. Virol. *80*, 1302–1310. 10.1128/JVI.80.3.1302-1310.2006.

59. Webb, S.R., Smith, S.E., Fried, M.G., and Dutch, R.E. (2018). Transmembrane domains of highly pathogenic viral fusion proteins exhibit trimeric association in vitro. mSphere *3*. 10.1128/mSphere.00047-18.

60. Barrett, C.T., and Dutch, R.E. (2020). Viral membrane fusion and the transmembrane domain. Viruses *12*. 10.3390/v12070693.

61. Jangra, S., Ye, C., Rathnasinghe, R., Stadlbauer, D., Personalized Virology Initiative study group, Krammer, F., Simon, V., Martinez-Sobrido, L., García-Sastre, A., and Schotsaert, M. (2021). SARS-CoV-2 spike E484K mutation reduces antibody neutralisation. Lancet Microbe *2*, e283–e284. 10.1016/S2666-5247(21)00068-9.

62. Gobeil, S.M.-C., Janowska, K., McDowell, S., Mansouri, K., Parks, R., Stalls, V., Kopp, M.F., Manne, K., Li, D., Wiehe, K., et al. (2021). Effect of natural mutations of SARS-CoV-2 on spike structure, conformation, and antigenicity. Science *373*. 10.1126/science.abi6226.

63. Chen, R.E., Zhang, X., Case, J.B., Winkler, E.S., Liu, Y., VanBlargan, L.A., Liu, J., Errico, J.M., Xie, X., Suryadevara, N., et al. (2021). Resistance of SARS-CoV-2 variants to neutralization by monoclonal and serum-derived polyclonal antibodies. Nat. Med. *27*, 717–726. 10.1038/s41591-021-01294-w.

64. Rappazzo, C.G., Tse, L.V., Kaku, C.I., Wrapp, D., Sakharkar, M., Huang, D., Deveau, L.M., Yockachonis, T.J., Herbert, A.S., Battles, M.B., et al. (2021). Broad and potent activity against SARS-like viruses by an engineered human monoclonal antibody. Science *371*, 823–829. 10.1126/science.abf4830.

65. Yuan, M., Zhu, X., He, W.-T., Zhou, P., Kaku, C.I., Capozzola, T., Zhu, C.Y., Yu, X., Liu, H., Yu, W., et al. (2022). A broad and potent neutralization epitope in SARS-related coronaviruses. Proc Natl Acad Sci USA *119*, e2205784119. 10.1073/pnas.2205784119.

66. Zhou, T., Tsybovsky, Y., Gorman, J., Rapp, M., Cerutti, G., Chuang, G.-Y., Katsamba, P.S., Sampson, J.M., Schön, A., Bimela, J., et al. (2020). Cryo-EM Structures of SARS-CoV-2 Spike without and with ACE2 Reveal a pH-Dependent Switch to Mediate Endosomal Positioning of Receptor-Binding Domains. Cell Host Microbe *28*, 867-879.e5. 10.1016/j.chom.2020.11.004.

67. Wrobel, A.G., Benton, D.J., Xu, P., Roustan, C., Martin, S.R., Rosenthal, P.B., Skehel, J.J., and Gamblin, S.J. (2020). SARS-CoV-2 and bat RaTG13 spike glycoprotein structures inform on virus evolution and furin-cleavage effects. Nat. Struct. Mol. Biol. *27*, 763–767. 10.1038/s41594-020-0468-7.

68. Wrobel, A.G., Benton, D.J., Xu, P., Calder, L.J., Borg, A., Roustan, C., Martin, S.R., Rosenthal, P.B., Skehel, J.J., and Gamblin, S.J. (2021). Structure and binding properties of Pangolin-CoV spike glycoprotein inform the evolution of SARS-CoV-2. Nat. Commun.

12, 837. 10.1038/s41467-021-21006-9.

69. Ray, D., Le, L., and Andricioaei, I. (2021). Distant residues modulate conformational opening in SARS-CoV-2 spike protein. Proc Natl Acad Sci USA *118*. 10.1073/pnas.2100943118.

70. Gobeil, S.M.-C., Janowska, K., McDowell, S., Mansouri, K., Parks, R., Manne, K., Stalls, V., Kopp, M.F., Henderson, R., Edwards, R.J., et al. (2021). D614G Mutation Alters SARS-CoV-2 Spike Conformation and Enhances Protease Cleavage at the S1/S2 Junction. Cell Rep. *34*, 108630. 10.1016/j.celrep.2020.108630.

71. Yurkovetskiy, L., Egri, S., Kurhade, C., Diaz-Salinas, M.A., Jaimes, J.A., Nyalile, T., Xie, X., Choudhary, M.C., Dauphin, A., Li, J.Z., et al. (2023). S:D614G and S:H655Y are gateway mutations that act epistatically to promote SARS-CoV-2 variant fitness. BioRxiv. 10.1101/2023.03.30.535005.

72. Liu, Y., Liu, J., Plante, K.S., Plante, J.A., Xie, X., Zhang, X., Ku, Z., An, Z., Scharton, D., Schindewolf, C., et al. (2022). The N501Y spike substitution enhances SARS-CoV-2 infection and transmission. Nature *602*, 294–299. 10.1038/s41586-021-04245-0.

73. Witte, L., Baharani, V.A., Schmidt, F., Wang, Z., Cho, A., Raspe, R., Guzman-Cardozo, C., Muecksch, F., Canis, M., Park, D.J., et al. (2023). Epistasis lowers the genetic barrier to SARS-CoV-2 neutralizing antibody escape. Nat. Commun. *14*, 302. 10.1038/s41467-023-35927-0.

74. Weisblum, Y., Schmidt, F., Zhang, F., DaSilva, J., Poston, D., Lorenzi, J.C., Muecksch, F., Rutkowska, M., Hoffmann, H.-H., Michailidis, E., et al. (2020). Escape from neutralizing antibodies by SARS-CoV-2 spike protein variants. eLife *9*. 10.7554/eLife.61312.

75. Wang, Q., Noettger, S., Xie, Q., Pastorio, C., Seidel, A., Müller, J.A., Jung, C., Jacob, T., Sparrer, K.M.J., Zech, F., et al. (2023). Determinants of species-specific utilization of ACE2 by human and animal coronaviruses. Commun. Biol. *6*, 1051. 10.1038/s42003-023-05436-3.

76. Zhang, K., Li, S., Pintilie, G., Chmielewski, D., Schmid, M.F., Simmons, G., Jin, J., and Chiu, W. (2020). A 3.4-Å cryo-electron microscopy structure of the human coronavirus spike trimer computationally derived from vitrified NL63 virus particles. QRB Discovery *1*, e11. 10.1017/qrd.2020.16.

77. Tortorici, M.A., Walls, A.C., Lang, Y., Wang, C., Li, Z., Koerhuis, D., Boons, G.-J., Bosch, B.-J., Rey, F.A., de Groot, R.J., et al. (2019). Structural basis for human coronavirus attachment to sialic acid receptors. Nat. Struct. Mol. Biol. *26*, 481–489. 10.1038/s41594-019-0233-y.

78. Song, X., Shi, Y., Ding, W., Niu, T., Sun, L., Tan, Y., Chen, Y., Shi, J., Xiong, Q., Huang, X., et al. (2021). Cryo-EM analysis of the HCoV-229E spike glycoprotein reveals dynamic prefusion conformational changes. Nat. Commun. *12*, 141. 10.1038/s41467-020-20401-y.

79. Li, Z., Tomlinson, A.C., Wong, A.H., Zhou, D., Desforges, M., Talbot, P.J., Benlekbir, S., Rubinstein, J.L., and Rini, J.M. (2019). The human coronavirus HCoV-229E S-protein structure and receptor binding. eLife *8*. 10.7554/eLife.51230.

80. Khaledian, E., Ulusan, S., Erickson, J., Fawcett, S., Letko, M.C., and Broschat, S.L. (2022). Sequence determinants of human-cell entry identified in ACE2-independent bat sarbecoviruses: A combined laboratory and computational network science approach. EBioMedicine *79*, 103990. 10.1016/j.ebiom.2022.103990.

81. Menachery, V.D., Dinnon, K.H., Yount, B.L., McAnarney, E.T., Gralinski, L.E., Hale, A., Graham, R.L., Scobey, T., Anthony, S.J., Wang, L., et al. (2020). Trypsin treatment unlocks barrier for zoonotic bat coronavirus infection. J. Virol. *94*. 10.1128/JVI.01774-19.

82. Seifert, S.N., Bai, S., Fawcett, S., Norton, E.B., Zwezdaryk, K.J., Robinson, J., Gunn, B., and Letko, M. (2022). An ACE2-dependent Sarbecovirus in Russian bats is resistant to SARS-CoV-2 vaccines. PLoS Pathog. *18*, e1010828. 10.1371/journal.ppat.1010828.

83. Walls, A.C., Tortorici, M.A., Snijder, J., Xiong, X., Bosch, B.-J., Rey, F.A., and Veesler, D. (2017). Tectonic conformational changes of a coronavirus spike glycoprotein promote membrane fusion. Proc Natl Acad Sci USA *114*, 11157–11162. 10.1073/pnas.1708727114.

84. Hofmann, M., and Wyler, R. (1988). Propagation of the virus of porcine epidemic diarrhea in cell culture. J. Clin. Microbiol. *26*, 2235–2239. 10.1128/jcm.26.11.2235-2239.1988.

85. Guo, H., Li, A., Dong, T.-Y., Si, H.-R., Hu, B., Li, B., Zhu, Y., Shi, Z.-L., and Letko, M. (2023). Isolation of ACE2-dependent and -independent sarbecoviruses from Chinese horseshoe bats. J. Virol. *97*, e0039523. 10.1128/jvi.00395-23.

86. Laporte, M., and Naesens, L. (2017). Airway proteases: an emerging drug target for influenza and other respiratory virus infections. Curr. Opin. Virol. *24*, 16–24. 10.1016/j.coviro.2017.03.018.

87. Hoffmann, M., Kleine-Weber, H., Schroeder, S., Krüger, N., Herrler, T., Erichsen, S., Schiergens, T.S., Herrler, G., Wu, N.-H., Nitsche, A., et al. (2020). SARS-CoV-2 Cell Entry Depends on ACE2 and TMPRSS2 and Is Blocked by a Clinically Proven Protease Inhibitor. Cell *181*, 271-280.e8. 10.1016/j.cell.2020.02.052.

88. Zhang, L., Cheng, H.-H., Krüger, N., Hörnich, B., Graichen, L., Hahn, A.S., Schulz, S.R., Jäck, H.-M., Stankov, M.V., Behrens, G.M.N., et al. (2024). ACE2-independent sarbecovirus cell entry is supported by TMPRSS2-related enzymes and reduces sensitivity to antibody-mediated neutralization. BioRxiv. 10.1101/2024.04.18.590061.

89. Hoffmann, M., Kleine-Weber, H., and Pöhlmann, S. (2020). A Multibasic Cleavage Site in the Spike Protein of SARS-CoV-2 Is Essential for Infection of Human Lung Cells. Mol. Cell *78*, 779-784.e5. 10.1016/j.molcel.2020.04.022.

90. Millet, J.K., and Whittaker, G.R. (2014). Host cell entry of Middle East respiratory syndrome coronavirus after two-step, furin-mediated activation of the spike protein. Proc Natl Acad Sci USA *111*, 15214–15219. 10.1073/pnas.1407087111.

91. Wu, Y., and Zhao, S. (2020). Furin cleavage sites naturally occur in coronaviruses. Stem Cell Res. *50*, 102115. 10.1016/j.scr.2020.102115.

92. Tang, T., Jaimes, J.A., Bidon, M.K., Straus, M.R., Daniel, S., and Whittaker, G.R. (2021). Proteolytic Activation of SARS-CoV-2 Spike at the S1/S2 Boundary: Potential Role of

Proteases beyond Furin. ACS Infect. Dis. *7*, 264–272. 10.1021/acsinfecdis.0c00701.

93. Laporte, M., Raeymaekers, V., Van Berwaer, R., Vandeput, J., Marchand-Casas, I., Thibaut, H.-J., Van Looveren, D., Martens, K., Hoffmann, M., Maes, P., et al. (2021). The SARS-CoV-2 and other human coronavirus spike proteins are fine-tuned towards temperature and proteases of the human airways. PLoS Pathog. *17*, e1009500. 10.1371/journal.ppat.1009500.

94. Peacock, T.P., Goldhill, D.H., Zhou, J., Baillon, L., Frise, R., Swann, O.C., Kugathasan, R., Penn, R., Brown, J.C., Sanchez-David, R.Y., et al. (2021). The furin cleavage site in the SARS-CoV-2 spike protein is required for transmission in ferrets. Nat. Microbiol. *6*, 899–909. 10.1038/s41564-021-00908-w.

95. Berger, I., and Schaffitzel, C. (2020). The SARS-CoV-2 spike protein: balancing stability and infectivity. Cell Res. *30*, 1059–1060. 10.1038/s41422-020-00430-4.

96. Zhang, S., Liang, Q., He, X., Zhao, C., Ren, W., Yang, Z., Wang, Z., Ding, Q., Deng, H., Wang, T., et al. (2022). Loss of Spike N370 glycosylation as an important evolutionary event for the enhanced infectivity of SARS-CoV-2. Cell Res. *32*, 315–318. 10.1038/s41422-021-00600-y.

97. Hirano, N., Fujiwara, K., Hino, S., and Matumoto, M. (1974). Replication and plaque formation of mouse hepatitis virus (MHV-2) in mouse cell line DBT culture. Arch. Gesamte Virusforsch. *44*, 298–302. 10.1007/bf01240618.

98. Chen, W., and Baric, R.S. (1996). Molecular anatomy of mouse hepatitis virus persistence: coevolution of increased host cell resistance and virus virulence. J. Virol. *70*, 3947–3960. 10.1128/JVI.70.6.3947-3960.1996.

99. Dieterle, M.E., Solà-Riera, C., Ye, C., Goodfellow, S.M., Mittler, E., Kasikci, E., Bradfute, S.B., Klingström, J., Jangra, R.K., and Chandran, K. (2021). Genetic depletion studies inform receptor usage by virulent hantaviruses in human endothelial cells. eLife *10*. 10.7554/eLife.69708.

100. Sievers, F., and Higgins, D.G. (2014). Clustal Omega, accurate alignment of very large numbers of sequences. Methods Mol. Biol. *1079*, 105–116. 10.1007/978-1-62703-646-7_6.

101. Takada, A., Robison, C., Goto, H., Sanchez, A., Murti, K.G., Whitt, M.A., and Kawaoka, Y. (1997). A system for functional analysis of Ebola virus glycoprotein. Proc Natl Acad Sci USA *94*, 14764–14769. 10.1073/pnas.94.26.14764.

102. Chandran, K., Sullivan, N.J., Felbor, U., Whelan, S.P., and Cunningham, J.M. (2005). Endosomal proteolysis of the Ebola virus glycoprotein is necessary for infection. Science *308*, 1643–1645. 10.1126/science.1110656.

103. Casalino, L., Gaieb, Z., Goldsmith, J.A., Hjorth, C.K., Dommer, A.C., Harbison, A.M., Fogarty, C.A., Barros, E.P., Taylor, B.C., McLellan, J.S., et al. (2020). Beyond Shielding: The Roles of Glycans in the SARS-CoV-2 Spike Protein. ACS Cent. Sci. *6*, 1722–1734. 10.1021/acscentsci.0c01056.

104. Punjani, A., Rubinstein, J.L., Fleet, D.J., and Brubaker, M.A. (2017). cryoSPARC:

algorithms for rapid unsupervised cryo-EM structure determination. Nat. Methods *14*, 290–296. 10.1038/nmeth.4169.

105. Pettersen, E.F., Goddard, T.D., Huang, C.C., Couch, G.S., Greenblatt, D.M., Meng, E.C., and Ferrin, T.E. (2004). UCSF Chimera—a visualization system for exploratory research and analysis. J. Comput. Chem. *25*, 1605–1612. 10.1002/jcc.20084.

106. Goddard, T.D., Huang, C.C., Meng, E.C., Pettersen, E.F., Couch, G.S., Morris, J.H., and Ferrin, T.E. (2018). UCSF ChimeraX: Meeting modern challenges in visualization and analysis. Protein Sci. *27*, 14–25. 10.1002/pro.3235.

107. Croll, T.I. (2018). ISOLDE: a physically realistic environment for model building into low-resolution electron-density maps. Acta Crystallogr. D Struct. Biol. *74*, 519–530. 10.1107/S2059798318002425.

108. Emsley, P., Lohkamp, B., Scott, W.G., and Cowtan, K. (2010). Features and development of Coot. Acta Crystallogr. D Biol. Crystallogr. *66*, 486–501. 10.1107/S0907444910007493.

109. Afonine, P.V., Poon, B.K., Read, R.J., Sobolev, O.V., Terwilliger, T.C., Urzhumtsev, A., and Adams, P.D. (2018). Real-space refinement in PHENIX for cryo-EM and crystallography. Acta Crystallogr. D Struct. Biol. *74*, 531–544. 10.1107/S2059798318006551.

110. Schwede, T., Kopp, J., Guex, N., and Peitsch, M.C. (2003). SWISS-MODEL: An automated protein homology-modeling server. Nucleic Acids Res. *31*, 3381–3385. 10.1093/nar/gkg520.

111. Jacobson, M.P., Pincus, D.L., Rapp, C.S., Day, T.J.F., Honig, B., Shaw, D.E., and Friesner, R.A. (2004). A hierarchical approach to all-atom protein loop prediction. Proteins *55*, 351–367. 10.1002/prot.10613.

112. Sali, A., and Blundell, T.L. (1993). Comparative protein modelling by satisfaction of spatial restraints. J. Mol. Biol. *234*, 779–815. 10.1006/jmbi.1993.1626.

113. Zhang, M., Gaschen, B., Blay, W., Foley, B., Haigwood, N., Kuiken, C., and Korber, B. (2004). Tracking global patterns of N-linked glycosylation site variation in highly variable viral glycoproteins: HIV, SIV, and HCV envelopes and influenza hemagglutinin. Glycobiology *14*, 1229–1246. 10.1093/glycob/cwh106.

114. Allen, J.D., Ivory, D.P., Song, S.G., He, W.-T., Capozzola, T., Yong, P., Burton, D.R., Andrabi, R., and Crispin, M. (2023). The diversity of the glycan shield of sarbecoviruses related to SARS-CoV-2. Cell Rep. *42*, 112307. 10.1016/j.celrep.2023.112307.

115. Watanabe, Y., Allen, J.D., Wrapp, D., McLellan, J.S., and Crispin, M. (2020). Site-specific glycan analysis of the SARS-CoV-2 spike. Science *369*, 330–333. 10.1126/science.abb9983.

116. Olsson, M.H.M., Søndergaard, C.R., Rostkowski, M., and Jensen, J.H. (2011). PROPKA3: Consistent Treatment of Internal and Surface Residues in Empirical pK Predictions. J. Chem. Theory Comput. *7*, 525–537. 10.1021/ct100578z.

117. Bland, R.D., Clarke, T.L., and Harden, L.B. (1976). Rapid infusion of sodium bicarbonate

and albumin into high-risk premature infants soon after birth: a controlled, prospective trial. Am. J. Obstet. Gynecol. *124*, 263–267. 10.1016/0002-9378(76)90154-x.

118. Guvench, O., Hatcher, E.R., Venable, R.M., Pastor, R.W., and Mackerell, A.D. (2009). CHARMM Additive All-Atom Force Field for Glycosidic Linkages between Hexopyranoses. J. Chem. Theory Comput. *5*, 2353–2370. 10.1021/ct900242e.

119. Huang, J., and MacKerell, A.D. (2013). CHARMM36 all-atom additive protein force field: validation based on comparison to NMR data. J. Comput. Chem. *34*, 2135–2145. 10.1002/jcc.23354.

120. Jorgensen, W.L., Chandrasekhar, J., Madura, J.D., Impey, R.W., and Klein, M.L. (1983). Comparison of simple potential functions for simulating liquid water. J. Chem. Phys. *79*, 926. 10.1063/1.445869.

121. Phillips, J.C., Hardy, D.J., Maia, J.D.C., Stone, J.E., Ribeiro, J.V., Bernardi, R.C., Buch, R., Fiorin, G., Hénin, J., Jiang, W., et al. (2020). Scalable molecular dynamics on CPU and GPU architectures with NAMD. J. Chem. Phys. *153*, 044130. 10.1063/5.0014475.

122. Guerois, R., Nielsen, J.E., and Serrano, L. (2002). Predicting changes in the stability of proteins and protein complexes: a study of more than 1000 mutations. J. Mol. Biol. *320*, 369–387. 10.1016/S0022-2836(02)00442-4.

123. Barlow, K.A., Ó Conchúir, S., Thompson, S., Suresh, P., Lucas, J.E., Heinonen, M., and Kortemme, T. (2018). Flex ddG: Rosetta Ensemble-Based Estimation of Changes in Protein-Protein Binding Affinity upon Mutation. J. Phys. Chem. B *122*, 5389–5399. 10.1021/acs.jpcb.7b11367.

Supplemental Figures

Supplementary File 1 - Nanopore sequencing of rVSV-SHC014 reveals A835D mutation. Related to Figure 1.

Supplementary File 2 - Nanopore sequencing of rVSV-SHC014 reveals F294L mutation. Related to Figure 7.

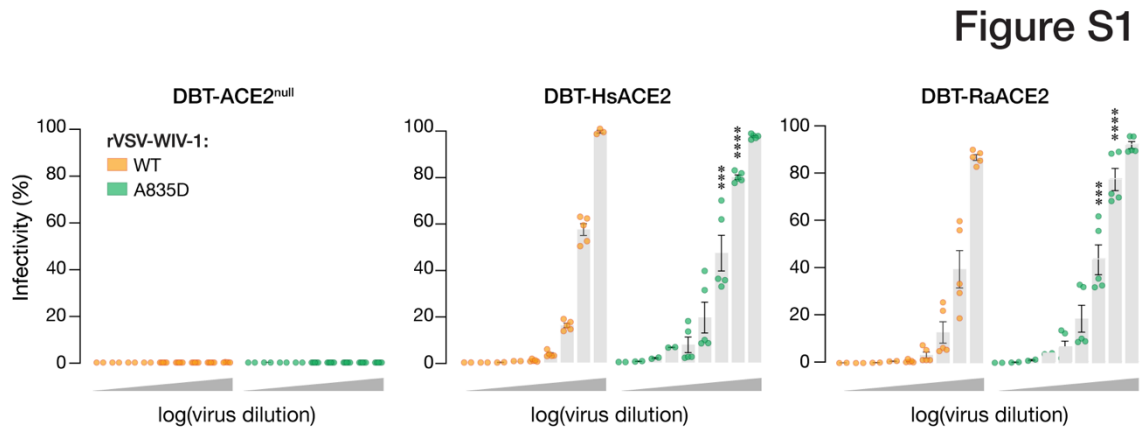

Figure S1 - rVSV-WIV-1 WT and A835D infection curves on DBT-9 cells overexpressing ACE2 orthologs. Related to Figure 2. Parental DBT-9 cells or DBT-9 cells overexpressing *Hs*ACE2 or *Ra*ACE2 were infected with rVSV-WIV-1 WT or A835D particles. Infection was scored by eGFP expression at 12 hours post-infection (average±SD, n=2–5 from 3 independent experiments). Groups (WT vs. mutant for each cell line) were compared with Welch's t-test with Holm-Šídák correction for multiple comparisons, ns $p>0.05$; ** $p<0.01$; *** $p<0.001$; **** $p<0.0001$. Only the statistically significant comparisons are shown.

Figure S2

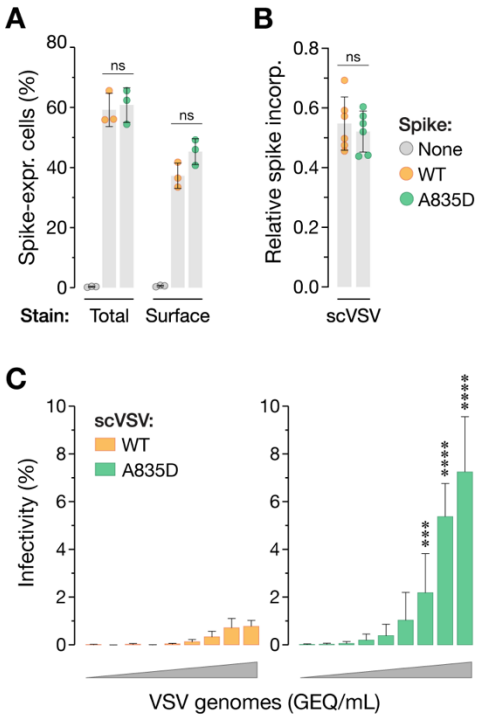

Figure S2 - A835D phenotype is independent of spike incorporation into VSV particles. Related to Figure 2. (a) 293FT cells were transfected with plasmids expressing WT or A835D SHC014 spike and immunostained for total protein expression (left) or cell surface expression (right) 24 hours post transfection by a spike-specific antibody and analyzed using flow cytometry (average±SD, n=3). Groups were compared by one-way ANOVA. **(b)** scVSV-SHC014-CoV S WT or A835D particles were coated on ELISA plates and probed with a spike-specific mAb or VSV M-specific mAb. The spike-to-M ratio demonstrates VSV particle-specific spike incorporation (average±SD, n=6 from 3 independent experiments). Groups were compared by one-way ANOVA. **(c)** Vero cells were infected with pre-titrated amounts of scVSV-SHC014-CoV S WT or A835D. Infection was scored by eGFP expression at 16–18 hours post-infection (average±SD, n=10-11 from 3 independent experiments). A range of 3.18×10^{1} to 1.24×10^{7} viral GEQ was used. Groups were compared with Welch's t-test with Holm-Šídák correction for multiple comparisons. ns $p>0.05$; ** $p<0.01$; *** $p<0.001$; **** $p<0.0001$. In panel c, only the statistically significant comparisons between WT and A835D are shown.

Figure S3

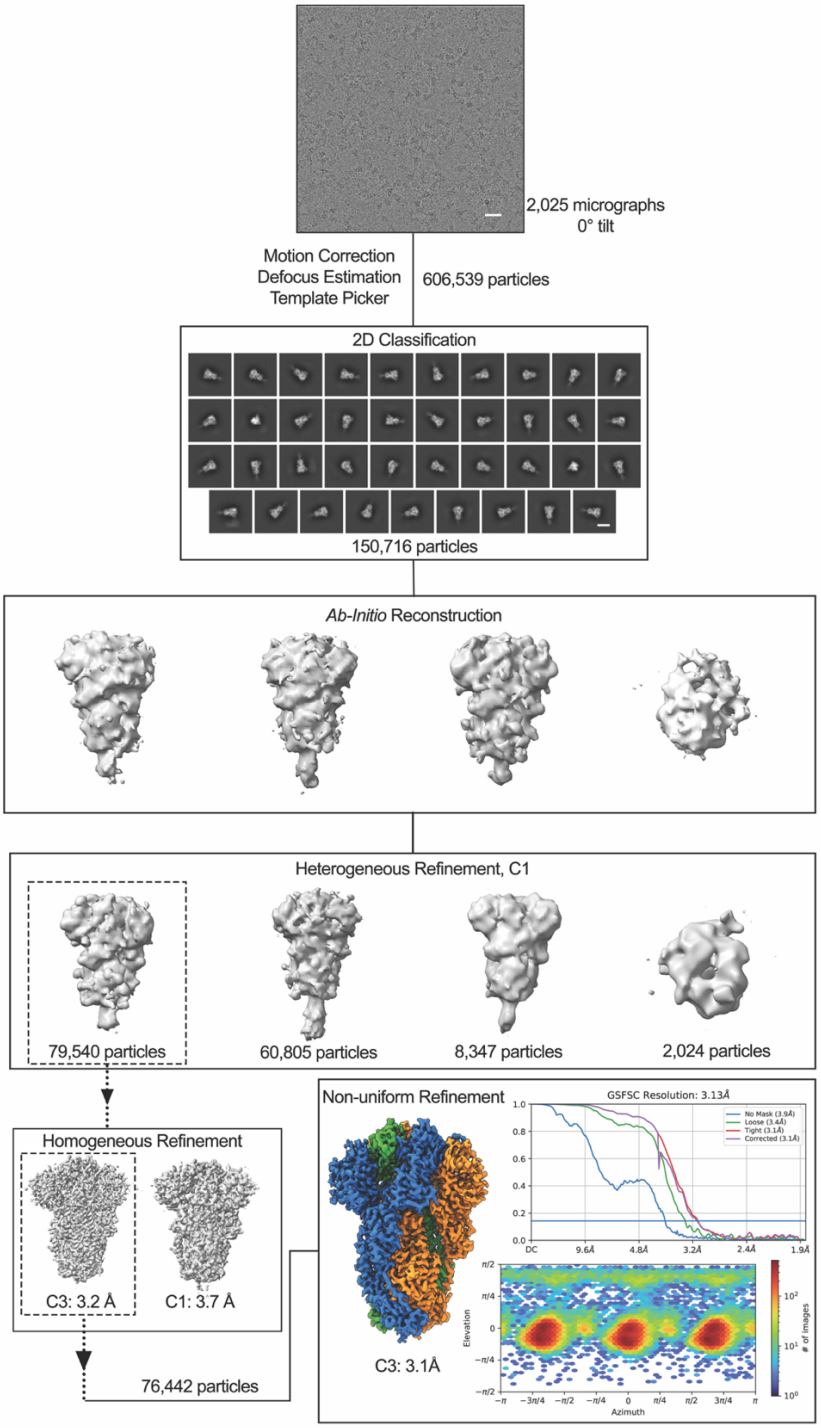

Figure S3 - Cryo-EM processing pipeline. Related to Figure 4. Cryo-EM processing workflow for the WT SHC014-CoV spike. The indicated steps were conducted using cryoSPARC v3: motion correction, contrast transfer function (CTF) estimation, 2D classification, heterogenous refinement, homogenous refinement with C3 symmetry imposed and non-uniform refinement with C3 symmetry imposed. Scale bars in micrograph and 2D classes represent 10 nm.

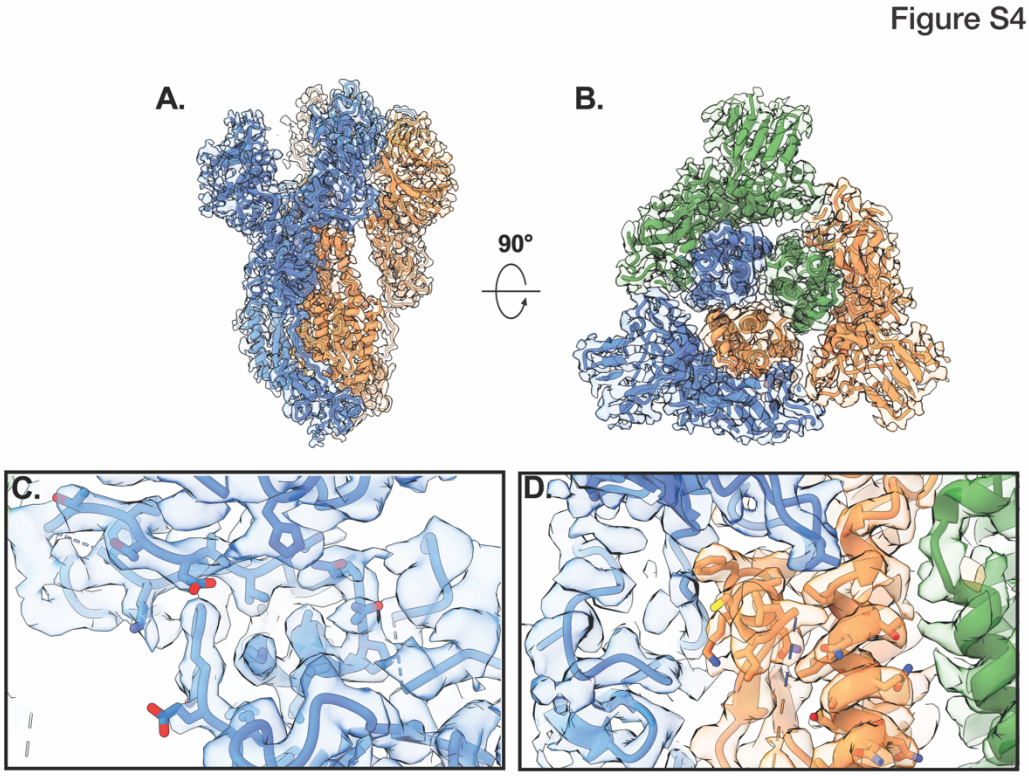

Figure S4 - Cryo-EM map-to-model fit. Related to Figure 4. Fit of the SHC014-CoV S model to the refined cryo-EM map. **(a)** Global map-to-model fit shown with one protomer hidden for clarity. **(b)** Global map-to-model fit z-slice with all protomers shown. **(c)** Local fit with side chains shown surrounding Phe294, with Lys266, Lys288, and Phe294 labelled. **(d)** Local fit with side chains shown surrounding Ala835, with Val556, Ala835, and Val946 labelled. For all panels, a threshold value of 0.19 was used to visualize the cryo-EM map.

Figure S5

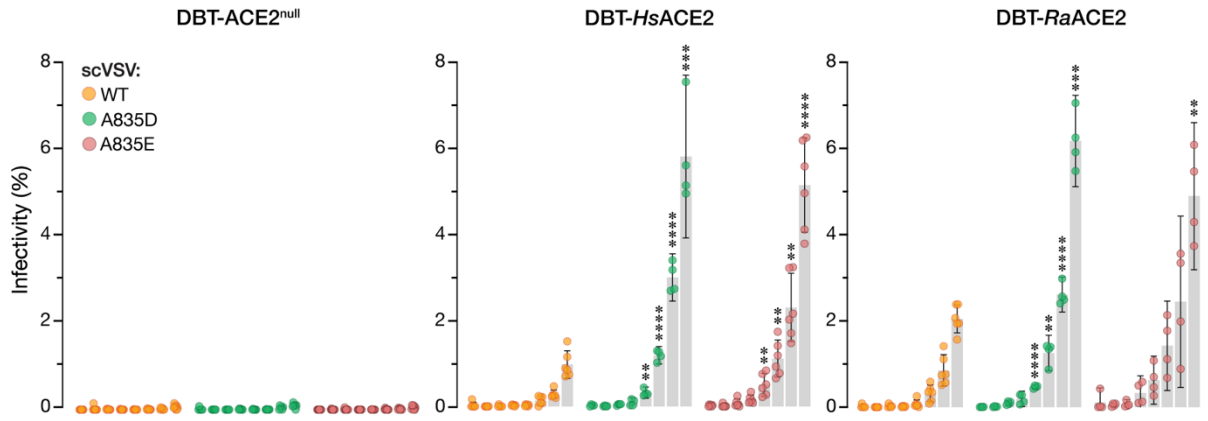

Figure S5 –scVSV-SHC014-CoV particles bearing A835E spikes have enhanced infectivity compared to WT. Related to Figure 4. Parental DBT-9 cells or DBT-9 cells overexpressing *Hs*ACE2 or *Ra*ACE2 were infected with pre-titrated amounts of scVSV-SHC014 particles bearing WT, A835D, or A835E spike. Infection was scored by eGFP expression at 16–18 hours post-infection (average±95%CI, n=4-8 from 2-3 independent experiments). A range of 4.6×10^{2} to 1.0×10^{6} viral GEQ was used. Groups (WT vs. mutant for each cell line) were compared with Welch's t-test with Holm-Šídák correction for multiple comparisons. ns $p>0.05$; ** $p<0.01$; *** $p<0.001$; **** $p<0.0001$. Only the statistically significant comparisons are shown.

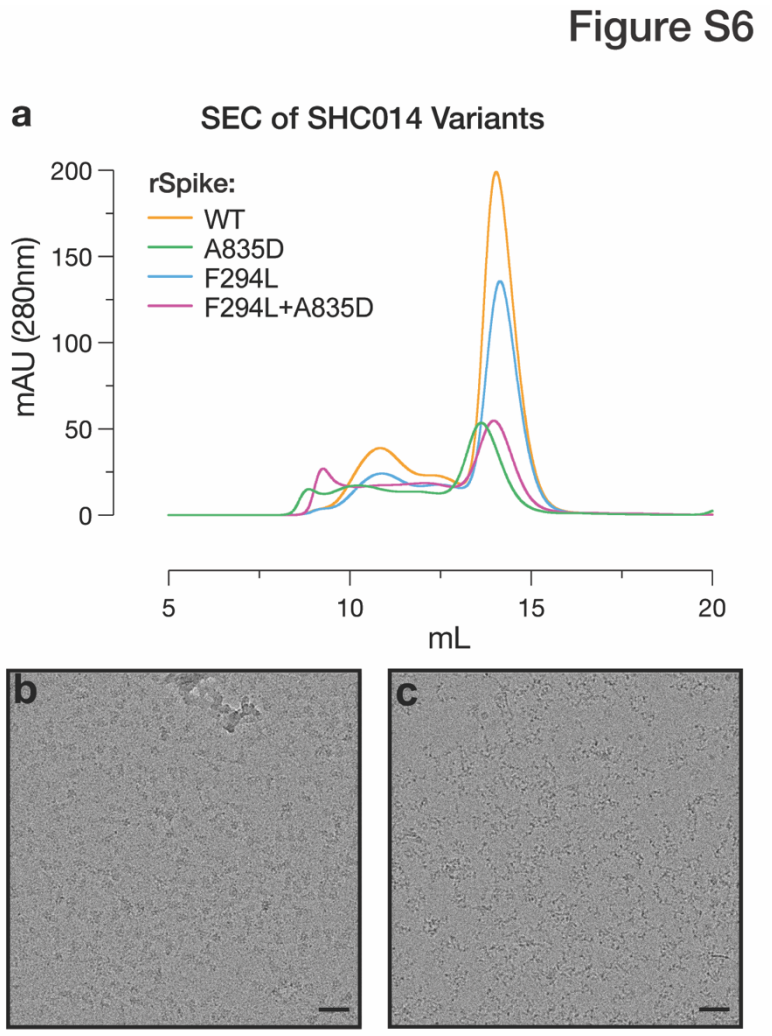

Figure S6 – Comparison of WT and mutant SHC014 CoV S ectodomains. Related to Figure 4. (a) Overlaid size-exclusion chromatography Abs_{280nm} traces show relative protein yield. WT, A835D, F284L, and F294L+A835D SHC014-CoV spikes were expressed and purified in tandem from the same cell line in the same culture volume. Area under the curve represents protein expression. A835D-containing variants exhibit a large decrease in protein expression relative to the WT and F294L SHC014-CoV spikes. **(b)** WT SHC014 CoV S visualized in a cryo-EM micrograph embedded in the vitreous ice. **(c)** A835D SHC014 visualized in a cryo-EM micrograph, prepared using the same protocol as in (a). Both spike proteins were expressed and purified at the same time using the same procedures. Scale bars in both represent 10 nm.

Figure S7

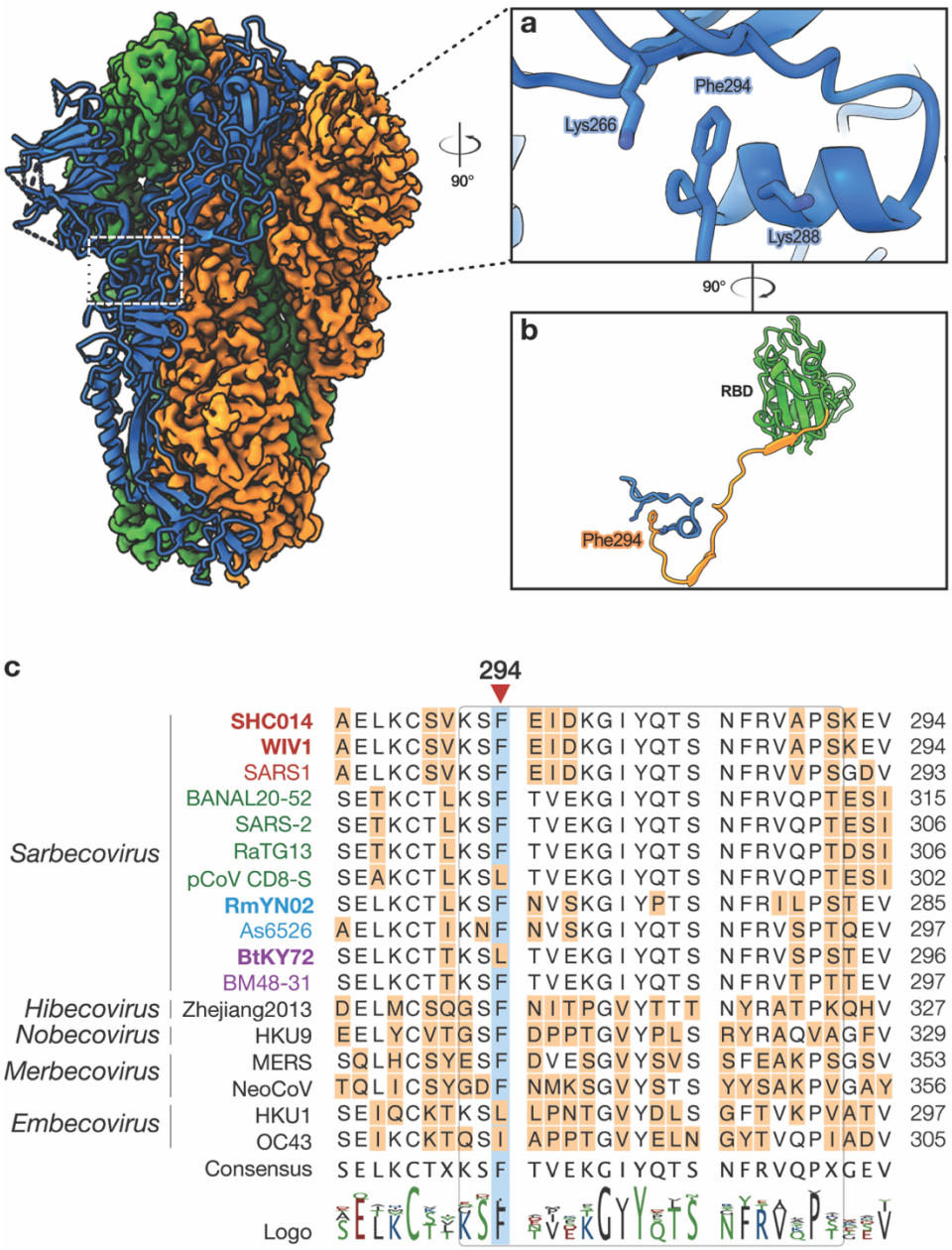

Figure S7 - Location and interactions of NTD mutation in SHC014-CoV spike. Related to Figure 7. (a) The aromatic ring of Phe294 is positioned between Lys266 and Lys288. **(b)** The distance between Phe294 and the RBD is depicted, with NTD residues and residues after SD1 hidden for clarity. Labelled residues are modeled as spheres. **(c)** Alignment of amino acid sequences in the F294 region (rounded rectangle) for selected coronavirus spike proteins. Subgenera are indicated in italics. Sarbecoviruses are color-coded by clade (1a: SARS-CoV–like, red; 1b: SARS-CoV-2–like, green; 2: Southeast Asian bat-origin CoV, blue; 3: non-Asian bat-origin CoV, purple). Spikes investigated in the current study are in bold.

Table S1. EM data collection, processing and refinement statistics

EM data collection	
Sample	Bat SARS-like CoV RsSHC014 S
Voltage (kV)	200
Detector	Falcon 4
Magnification (nominal)	105,000
Pixel size (Å/pix)	0.94
Exposure rate (e^-/pix/sec)	3.40
Frames per exposure	50
Exposure (e^-/Å^2)	50
Defocus range (μm)	1.0-2.0
Tilt angle (˚)	0
Micrographs collected	2,025
Micrographs used	1,097
Particles extracted (total)	419,182
Automation software	SerialEM
3D reconstruction statistics	
Particles	76,442
Symmetry	C3
Map sharpening B-factor	-82.8
Unmasked resolution at 0.5 FSC (Å)	7.5
Masked resolution at 0.5 FSC (Å)	3.7
Unmasked resolution at 0.143 FSC (Å)	3.9
Masked resolution at 0.143 FSC (Å)	3.1
Model refinement and validation statistics	
Refinement package	Phenix
Composition	
Amino acids	2,925
RMSD bonds (Å)	0.005
RMSD angles (º)	0.98
Average B-factors	
Amino acids	71.2
Ramachandran	
Favored (%)	96.0
Allowed (%)	4.0
Outliers (%)	0.0
Rotamer outliers (%)	0.47
Clash score	5.84
C-beta outliers (%)	0
CaBLAM outliers (%)	3.12
CC (mask)	0.78

MolProbity score	1.59